Analysis of the Data Quality of the FTT

Diplomarbeit
am
Lehrstuhl für Experimentelle Physik V
der
Universität Dortmund

vorgelegt von
Dirk Dodt

März 2005

abstract

In order to take most advantage from the HERA II luminosity upgrade, the trigger system of the H1 detector is being improved. Besides other measures this includes the implementation of a new fast track trigger (FTT) that uses information of the central drift chambers of H1. The aim of this work was to help during the commissioning of the FTT and to provide some tools for the analysis of the monitoring data of the FTT system. A graphical display for the FTT front end was written. Tools measuring the hit finding efficiency with various methods were implemented. The drift time information of the FTT hits were calibrated taking into account a T_0 offset determined per wire, the chamber alignment and variations of the drift velocity and Lorentz angle. The effective wire lengths and z shifts needed for the determination of the z coordinate by charge division are measured in a second calibration procedure.

Contents

1. Introduction

The HERA electron proton scattering experiments are the sequel of a long series of successful efforts to investigate the structure of the proton. Since the early 1950s physicists facilitated lepton beams to probe atomic nuclei and in particular protons. These measurements were mainly analysed in terms of structure functions, expressing information about the angular and energetic distributions of the scattered particles[1]. This formalism comprises some analogy to the connection between the intensity distribution of light, that has been diffracted e.g. by a slit and the shape of the slit itself. The spatial resolution to which structures can be investigated is, just as in the analogy of diffracted light, determined by the wavelength of the scattered radiation. In deep inelastic lepton proton scattering (DIS) this is given by the de Broglie wavelength λ_m of the gauge boson mediating the interaction. As λ_m is inverse proportional to the momentum transfer involved in the scattering reaction, historically the experiments always aimed at the highest possible beam energy [1, 2].

In this chapter a brief overview over the historical development of proton structure measurements is given, in order to illustrate the context of HERA physics.

1.1. Historical Overview

1.1.1. Evidence of Spatial Extension from Elastic Scattering

The first evidence for a substructure of the proton was obtained by the MARK III linear accelerator in Stanford [3, 4]. During the early 1950s Hofstadter et al. investigated the elastic scattering of a 400 MeV electron beam on fixed target nuclei and protons. A spatial resolution of $\lambda_m \sim \hbar/p \approx 0.5\,\mathrm{fm}$ was achieved in these experiments. The electric and magnetic form factors obtained from the differential cross section were compatible with a charge distribution having a size of $\sim$0.75 fm rather than a point-like proton.

1.1.2. Point-Like Constituents in Inelastic Scattering, the Quark Parton Model

The progress of accelerator physics allowed for a fast increase of the beam energy by almost two orders of magnitude within about 15 years. In 1967 a new linear accelerator at Stanford achieved an electron beam energy of 17 GeV (corresponding to roughly 0.01 fm spatial resolution capability).

At these energies the proton is likely to break up into jets of secondary particles during the scattering process. The electron only interacts with a fraction of the proton, not with the whole particle. The ignorance of the actual scattering partner gives rise to a substantial change of the kinematics of the process. In *elastic* scattering there is only one non-trivial degree of freedom[2], reflecting the unknown impact parameter of the scattering process. This means the differential cross section can be parametrized as function of only one free parameter. However in *inelastic* reactions a second degree of freedom is present. It is connected to the mass/momentum of the initial state or in other words the energy transfer involved in the interaction, respectively.

[1] As it will be discussed below, it is sufficient to consider the angular and energetic distribution of the scattered lepton, compare paragraph 1.2.1.

[2] Assuming head-on collisions at fixed beam energies.

The experiments at Stanford observed an *elastic-like* behaviour in *inelastic* reactions, which was referred to as 'scaling'[3] [5, 6] and had been predicted by Bjorken [7]. Feynman explained this result as the elastic scattering on *quasi free*, point-like constituents of the proton [8]. In 1969 Bjorken and Paschos [9] associated the *partons* with the quarks of the static quark model. The *static* quark model had been formulated in the early 1960s by Gell-Mann and Zweig. It classifies the bulk of particles produced in high energy collisions on the basis of approximate group theoretical symmetries observed in terms of spin and isospin characteristics.

1.1.3. Scaling Violations in DIS, the QCD Proton

A further increase in resolution capabilities showed the limits of this attractively simple model. The electrically charged partons were measured to carry only half of the momentum of the proton [10] and the scaling behaviour turned out to be violated at shorter wavelengths [11].

An explanation for these and further phenomena is given by the gauge field theory of strong interactions, quantum chromodynamics (*QCD*). QCD was successfully formulated in 1973 and describes the interactions of the quarks. The term chromodynamics is connected to the 'charge' of the strong interaction, which is called *colour*.

A new category of proton constituents was introduced in the framework of QCD: the *gluons*. The gluon is the mediator of the strong interaction just as the photon mediates the electromagnetic interaction. The momentum fraction of the proton that is not carried by the charged partons has to be attributed to the existence of gluons. Also the scaling violation of the structure functions can be well described when taking into account the implications of the gluon content of the proton [12].

The gluons are able to fluctuate into a quark - antiquark pair for a short time, exactly as a photon is able to fluctuate into an electron - positron pair. These fluctuations build up the so called *sea quarks* inside the proton. They are observed in addition to the *valence quarks,* that define the properties of the proton in terms of the static quark model.

In contrast to the electrically neutral photons, gluons carry colour. This fact has many implications on the nature of the strong interaction. It is the reason for the increase of the strong force with rising distance, and in particular forbids the observation of free quarks or gluons.

1.2. Measurements at HERA

The usage of colliding beams allowed for a substantial extension of the kinematic range previously explored by fixed target experiments. This makes HERA an unique laboratory for the exploration of the structure of the proton and allows for a precise test of QCD predictions.

1.2.1. Kinematics and Terminology

In deep inelastic scattering at HERA electrons are scattered off protons, at momenta where both rest masses are negligible in first approximation. The interaction can be described in terms of the exchange of a virtual gauge boson in leading order. The exchange of a photon γ or Z^0 boson is called neutral current reaction and does not affect the nature of the probing lepton. In charged current reactions, mediated by a W^+or W^-boson, a neutrino is emitted. The scattered proton dissociates into the hadronic final state called X.

[3]The term 'scaling' or 'scale invariance' arises from the fact, that the differential cross section does not depend on the resolution of the scattering process.

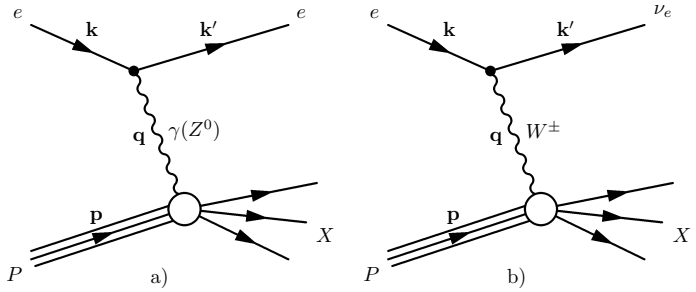

particle	momentum
electron e	k
scattered lepton e, ν_e	k'
gauge boson γ, Z^0,$W^\pm$	q
proton P	p
hadronic final state X	

Figure 1.1.: Leading order processes of ep scattering: neutral and charged current reactions. All momenta are used in form of relativistic four vectors.

The description and observation of DIS interactions is usually performed in terms of the Lorentz invariant quantities given below:

- The square of the energy in the center of mass frame s; which is defined by the energies of the colliding beams
$$s = (p + k)^2.$$
- The negative square of the four momentum transfer at the electron vertex (sometimes expressed as Mandelstam variable t)
$$Q^2 = -q^2 = -(k - k')^2$$
- The Bjorken scaling variable x; in the context of the parton model x is interpreted as the fraction of proton momentum, carried by the struck quark in the proton infinite momentum frame. Henceforth x fulfills $0 \leq x \leq 1$.
$$x = \frac{Q^2}{2p \cdot q}$$
- The inelasticity y; in the rest frame of the proton y describes the fraction of the energy of the electron being transferred during the interaction. Also for y the rule $0 \leq y \leq 1$ holds.
$$y = \frac{p \cdot q}{p \cdot k} = \frac{t}{s}.$$

The equation $Q^2 = sxy$, holding for neglected particle rest masses reduces the number of independent kinematical parameters to two. This reflects the number of the two degrees of freedom in inelastic scattering mentioned above.

Form Factors and Structure Functions Obtaining structure information by scattering an electron off an unknown charged object, is a well-proved technique. The standard practice is to compare the angular distribution $\frac{d\sigma}{dQ^2}$ of the scattered electrons to the known cross section of a point charge $\left(\frac{d\sigma}{dQ^2}\right)_{\text{point}}$
$$\frac{d\sigma}{dQ^2} = \left(\frac{d\sigma}{dQ^2}\right)_{\text{point}} |F(q)|^2 .$$

All structure information is contained in the form factor $F(q)$. In case of a static target $F(q)$ can be shown to be the Fourier transform of the probed charge distribution [2].

The above expression can be generalized to the problem of proton structure functions. To achieve this the magnetic moment of the proton, the recoil of the target and the inelastic nature of the scattering have to be taken into account. Using the lowest order (Born approximation) and only the electromagnetic part of the cross section one yields

$$\frac{d^2\sigma_{\mathrm{Born}}}{dx\,dQ^2} = \frac{4\pi\alpha_{\mathrm{em}}^2}{x\,Q^4}\left(y^2 x\,F_1(x,Q^2) + (1-y)\,F_2(x,Q^2)\right).$$

α_{em} is the electromagnetic coupling constant and F_1 and F_2 are the desired proton structure functions. At high four momentum transfers additional terms are necessary accounting for the Z^0 exchange and interference between the couplings.

In ep interactions at all except for the lowest Q^2 the proton is very likely to dissociate into the hadronic final state X. The energy transfer in the reaction forbids the direct extraction of the spatial structure possible in the static case mentioned above. Instead the structure functions are interpreted in terms of effective quark density functions $q_i(x,Q^2)$ and $\bar{q}_i(x,Q^2)$, describing the probability of scattering off a quark or antiquark of flavour i and with fractional proton momentum x.

$$F_2(x,Q^2) = \sum_{i=1}^{n_f} e_i^2 x\left(q_i(x,Q^2) + \bar{q}_i(x,Q^2)\right).$$

The fact that F_2 decomposes into a sum of probabilities instead of quantum amplitudes reflects the assumption of incoherent scattering off the different partons. The Q^2 dependence of the parton densities, that is violating scaling behaviour, can be described in QCD and is connected to the possibility of gluon emission by the quarks. While it is possible to compute the evolution of the quark and gluon densities with rising Q^2, their absolute values can't be predicted. The equations decribing the evolution have to be adapted to the F_2 data in so called QCD fits.

1.2.2. Inclusive Analysis

The measurement of the proton structure functions is called *inclusive* because the kinematic distribution of all different final states is analysed. F_2 is extracted from the measured inclusive cross section, figure 1.2. For scattering on spin half partons (quarks) the Callan Gross relation $F_1 = 2x \cdot F_2$ [13] is valid. Deviations from this approximately fulfilled behaviour are expressed using the structure functions F_L and F_3. The generalized structure function F_3 is obtained from the difference between e^+p and e^-p cross sections. The longitudinal structure function F_L is extracted from the difference of the cross section to the extrapolation of F_2 to kinematical regions were the influence of F_L is not negligible (high y) [12].

The parton densities and the strong coupling constants α_s are obtained from a fit of QCD models of the structure functions to the data [12]. The gluon density g resulting from the fits turns out to depend on the underlying model [14]. It can be obtained in an independent way from *semi-inclusive* measurements.

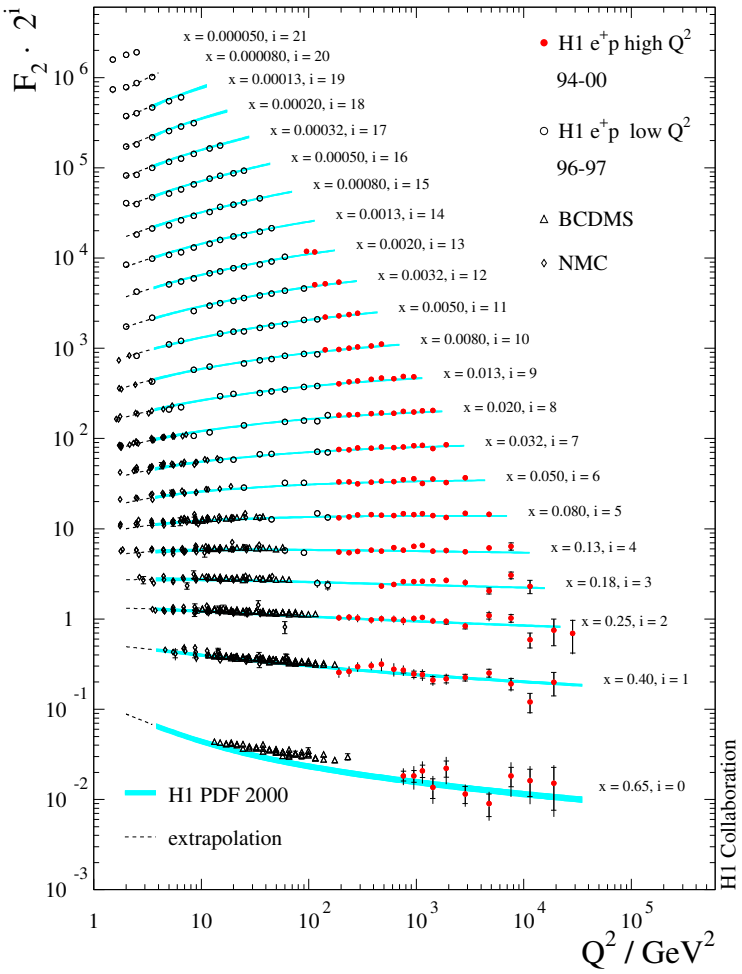

Figure 1.2.: H1 result of the data taking period 94-00 for the proton structure function F_2 is shown as function of Q^2 for different bins of x. The blue areas are the error bands of a fit to QCD evolution predictions (H1 PDF 2000)[12].

1.2.3. Semi-Inclusive Analysis

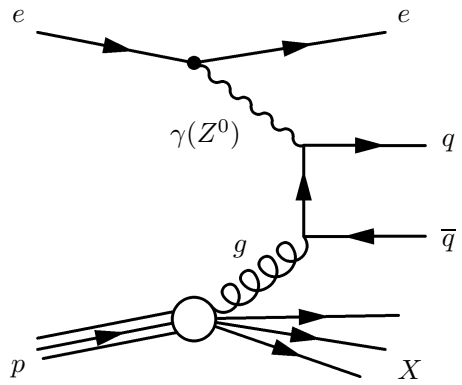

particle
electron e
intermediating boson γ, Z_0
quark antiquark pair q, $\bar{q}$
gluon g
proton P
hadronic final state X

Figure 1.3.: Graph of the production of a quark - antiquark pair in a boson gluon fusion process.

In semi-inclusive analyses only a certain class of events is taken into account. This class is defined by containing a specific particle in the final state of the scattering reaction. For example the cross section of open charm (D^*) production in ep scattering is measured at HERA. The D^* production can be interpreted in terms of its contribution to F_2 which is called $F_2^{c\bar{c}}$.

The D^* contains a heavy quark inexistent in the valence quarks of the proton. That is why its production can primarily be attributed to quark - antiquark fluctuations of gluons inside the proton. The main production process [15], which is called boson gluon fusion (bgf) is shown in figure 1.3.

The D^* production cross section is a sensitive probe to the gluon density distribution [15]. It is used to obtain independent result for g that is compared to the results from inclusive QCD fits using different approaches.

In principle the same is true for the production cross section of the J/Ψ vector meson, which is composed of two heavy quarks. Uncertainties in the knowledge of the precise production mechanism however complicate the interpretation of the J/Ψ cross section.

2. The H1 Detector at HERA

2.1. HERA Storage Rings

The HERA (Hadron Elektron Ring Anlage = hadron electron ring facility) consists of two storage rings with a circumference of 6.3 km length. Bunches of polarized electrons or positrons[1] with an energy of 27.5 GeV are brought to collision with 920 GeV proton bunches inside the two detectors H1 and ZEUS. The bunch crossing frequency is 10.4 MHz. The fixed target experiment HERMES is colliding the lepton beam with polarized gas targets measuring the spin structure of nucleons and nuclei. The HERA-B experiment was taking data for heavy quark physics until the year 2003 using wire targets exposed to the halo of the proton beam.

2.1.1. HERA-II Luminosity Upgrade

The rate n at which a given processes with cross section σ occurs is determined by the luminosity $\mathcal{L}$ of the collider experiment

$$n = \mathcal{L} \cdot \sigma.$$

At the end of 2000 a sizable amount of inclusive data was available for the determination of F_2 in a wide range of x and Q^2. At the highest values of Q^2 however the uncertainties of F_2 were dominated by the effect of low statistics. Also the measurements of heavy quark production and other low cross section processes were statistically limited. It was decided that an efficient measurement of these processes requires a significant increase of the luminosity.

2.1.2. Machine Aspects of the Upgrade

The luminosity delivered by an accelerator depends on the product of the beam currents $I_e \cdot I_p$ and the smallness of the transverse beam sizes $\sigma_x \cdot \sigma_y$ at the interaction points (IP).

$$\mathcal{L} \propto \frac{I_e \cdot I_p}{\sigma_x \cdot \sigma_y}$$

For HERA-II a decrease of the beam sizes was preferred over enhancing the beam currents. An increase of the beam currents would have required an extension of the high frequency system of the electron beam or extensive changes in the magnet structure of the proton pre-accelerators.

The *proton beam size* is reduced by moving the (warm) half quadrupole magnets, that are responsible for the final focusing closer to the IP. This necessitates an earlier separation of the head on[2] colliding beams, requiring an increased dipole field in the interaction region. The more intense synchrotron radiation that is emitted due to the higher field is guided outside the detectors in a dedicated beam pipe.

The *electron beam size*, that has to match the proton beam size, is first of all reduced by using superconducting combined function magnets. These enhance the final focusing and provide the increased separation dipole field. The superconducting technique has the advantage of not

[1] From here on the term electron is used synonymously for both electrons and positrons.

[2] Head on geometry utilises the momentum dependency of the bending radius in a magnetic dipole field to collide and separate particle beams with different particles. (In contrast to crossing angle geometry)

Table 2.1.: Detector components in figure 2.1

number	Detector Component
1	interaction point (IP)
2	central silicon tracker (CST)
3	backward silicon tracker (BST)
4	forward silicon tracker (FST)
5	central inner proportional chamber (CIP 2000)
6	central outer proportional chamber (COP)
7	central jet chamber 1 (CJC1)
8	central jet chamber 2 (CJC2)
9	forward tracking detector (FTD)
10	backward proportional chamber (BPC)
11	liquid argon cryostat
12	liquid argon calorimeter, elm. (LAr)
13	liquid argon calorimeter, hadronic
14	spaghetti calorimeter, elm. (SpaCal)
15	spaghetti calorimeter
16	superconducting GG magnet
17	superconducting GO magnet
18	superconducting field coil
19	central muon system (CMS)
20	muon toroid magnet
21	forward muon detector (FMD)

needing an iron field return yoke. For this reason the magnets could be built with a large aperture and small outer diameter.

Secondly the electron optic is optimized for a lower horizontal emittance. The emittance is a measure for the conserved phase space volume occupied by the beam. It determines the beam size together with the magnetic focusing at a given part of the storage ring. In case of electrons the emittance is controlled by the damping conditions, which were adjusted for HERA-II [16, 17].

Another issue is the *polarisation* of the electron beam. Provided a "spin matched" optic the emission of synchrotron photons leads to an intrinsic polarisation. This transverse polarization has to be turned longitudinal by spin rotators around the experiments in order to be useful e.g. to measure helicity dependent weak interaction physics. The HERMES experiment used to have a spin rotator installed already since 1994. During the HERA-II upgrade spin rotators were also installed for H1 and ZEUS. During 2004 the longitudinal polarization delivered in the presence of collisions was around 40% to 50% [18].

2.2. H1 Detector

The H1 Detector is a large (about $12\,\mathrm{m} \cdot 10\,\mathrm{m} \cdot 15\,\mathrm{m}$, 2800 t) multipurpose detector with a near to 4π acceptance and is equipped with tracking, calorimetric and muon detectors. The instrumentation and in particular the calorimeter is enhanced in proton direction, because of the imbalanced beam energies. A superconducting coil provides a 1.15T magnetic field allowing for track momentum measurement. The coil is enclosing the calorimeters and thus minimizing the amount of dead material in front of the calorimeters. The detector was designed for *good*

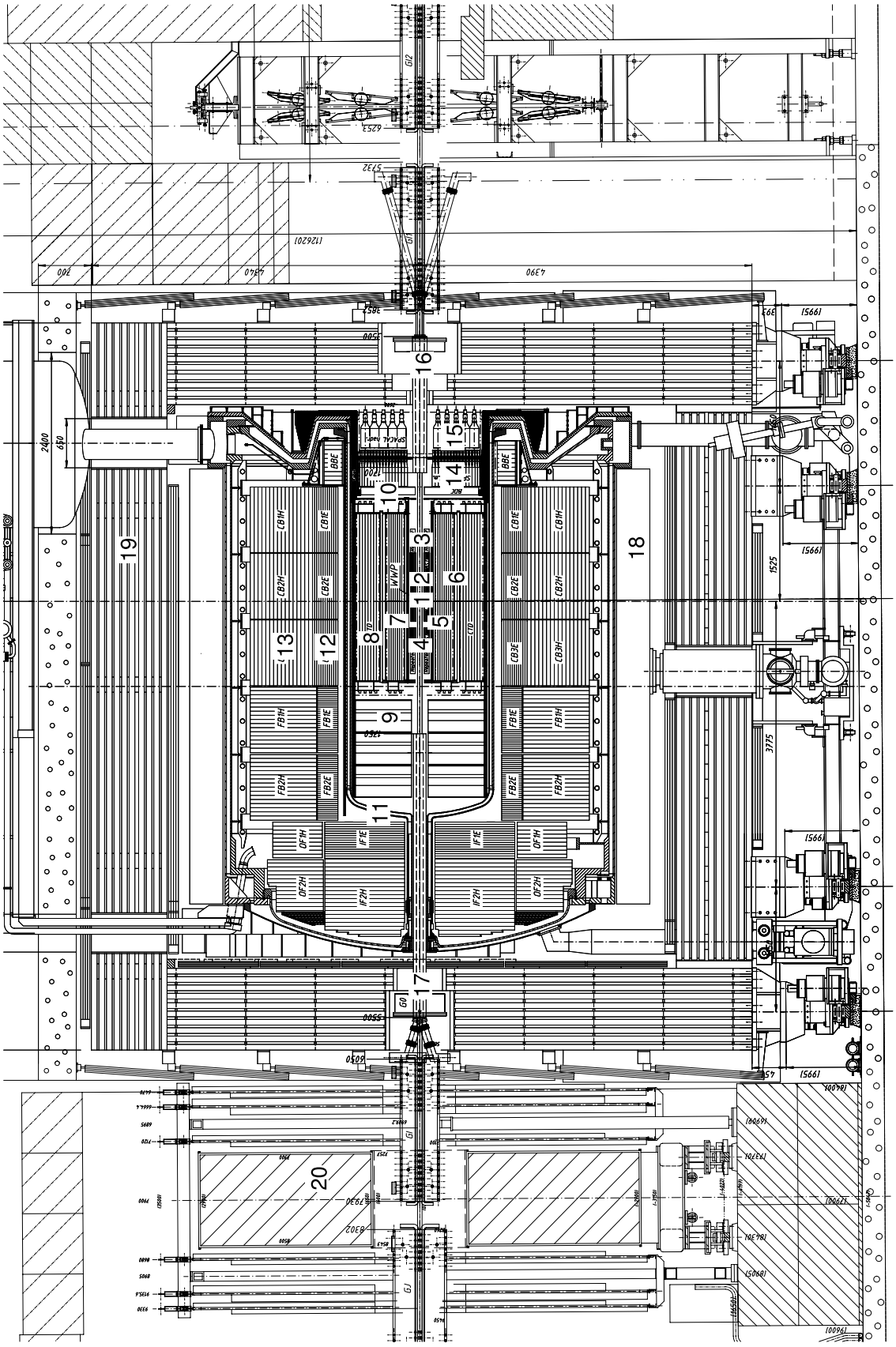

Figure 2.1.: Side view of the H1 detector.

identification of electrons and muons, *high resolution capability* for the hadronic final state as well as *full solid angle coverage* for detection of missing energy (neutrinos). Particle identification is provided through means of calorimetric shower shape (electrons and hadrons) and through the instrumented return yoke and forward muon toroid (muons). Also the energy loss ($\frac{dE}{dx}$) measured in the central tracking chamber can be utilized to some extend to identify particles [19, 20].

The description of detector components given here is referring to the status after the HERA-II upgrade. The calorimetric and muon system of H1 are briefly introduced in the next paragraphs. The tracking system and especially the central tracking chambers are discussed in more detail, because of their importance for this thesis.

coordinate system the right handed *cartesic coordinate* system used for the description of the detector is defined as follows: the proton beam heads in positive z direction while the x axis points to the center of the storage ring. Consequently the positive y direction points upwards. Where *polar coordinates* are used the azimuthal angle φ is defined in the x-y plane, $\varphi = 0$ meaning parallel to the x axis. The polar angle θ is defined with respect to the beam axis, $\theta = 0$ corresponding to the proton beam direction.

2.2.1. Calorimetry

The most important calorimeters of H1 are liquid argon (LAr) calorimeter covering the forward and central region and the backward scintillating fibre (SpaCal) calorimeter. The polar angle coverage and other design parameters are summarized in table 2.2.

The *LAr* sampling calorimeter technology has the advantages of a good stability, easy calibration and fine granularity necessary for electron and pion separation. The H1 LAr is divided into the inner so called electromagnetic (elm) section (lead converter) and the outer hadronic part (stainless steal converter). The fine segmentation of the calorimeter and its readout allows for software correction of the intrinsically different response to electrons and hadrons (pions) with the same energy. It also provides good spatial resolution which is essential for the precise reconstruction of the event kinematic. The problem of the slow signal formation times of LAr calorimeters is overcome by signal shaping electronics, allowing to use the LAr as source of trigger information (compare section 2.3) [21].

The so called *spaghetti calorimeter* of H1 consists of scintillating fibres embedded into a matrix made of lead. Its main purpose is the precise measurement of the scattered electron in low- or medium-Q^2 events. Similar to the LAr the electron identification is possible through means of shower shape variables enabled by the fine granularity of the readout. Its fast response ($\sim$ 1ns [22]) also qualifies the SpaCal to deliver valuable information to the Time-Of-Flight (TOF) sensitive trigger, vetoing a significant fraction of the proton beam induced background.[23, 24]

2.2.2. Muon System

The magnetic flux of the superconducting coil enclosing the calorimeters of H1 is guided back in an iron return yoke building the outermost layer of H1. The yoke is instrumented with 16 streamer tube layers for the detection of muons (CMD). In forward direction the forward muon detector (FMD) is installed with a polar angle coverage between 3°and 17°. A toroidal magnet provides a magnetic field of 1.6 T allowing momentum measurement in the FMD. Most of the muons created in ep interactions penetrate through the calorimeter and are measured in the muon system. The muon systems deliver information to the H1 trigger system.

	Liquid Argon	SpaCal
polar angle coverage	$4^\circ < \Theta < 154^\circ$	$155^\circ < \Theta < 174^\circ$
active material	LAr	Scintillating fibres
converter	lead/stainless steel	lead
thickness electromagnetic	20 - 30 radiation lengths	28 radiation lengths
thickness hadronic	5 - 8 absorptions lengths	1 absorption length
readout cells (elm/hadronic)	30784/13568	1192/136
relative energy resolution		
for electrons (elm)	$12\%/\sqrt{E} \oplus 1\%$	$7.1\%/\sqrt{E} \oplus 1\%$
for pions (hadronic)	$50\%/\sqrt{E} \oplus 2\%$	–

Table 2.2.: Design and performance parameters of the H1 calorimeters [25, 20].

2.2.3. Tracking

The tracking system of the H1 detector is designed for the reconstruction of jets with high particle densities, requiring a good double track resolution of ~ 2.5mm ($\hat{=}$50ns drift time). The design resolutions are $\frac{\sigma_{p_t}}{p_t} \sim 3 \times 10^{-3} \cdot p_t$ (momentum) and $\sigma_\theta \sim 1$ mrad (polar angle) [19, 20]. The track reconstruction is based on two concentric drift chambers of the jet chamber type covering a polar angle range of $25^\circ < \Theta < 155^\circ$. Because of the preferred forward emission of the hadronic final state the CJCs are supplemented by the forward tracking detectors (FTD, acceptance $7^\circ < \Theta < 25^\circ$). The FTD extends the polar angle with full track length in the plane orthogonal to the magnetic field down to polar angles of $\theta \sim 15^\circ$. Downstream of the interaction point the backward proportional chamber (BPC, 6 layers) provides spatial information about the back scattered electron, whose energy is measured in the SpaCal. The track measurement is completed by the information from subsystems briefly described here:

- The central, forward and backward silicon trackers (CST, FST, BST) being the innermost track detectors are used to obtain precise information about the origin of tracks. They allow the identification of secondary vertices and the forward and backward systems provide information for tracks at high and low polar angles.
- The central inner and outer proportional chambers (CIP and COP) provide fast signals used in the trigger system. The CIP provides information for a z vertex trigger used to suppress proton induced background.
- The central outer z chamber (COZ) provides precise z information.

Because of their importance for this thesis the central jet chambers are discussed in some detail in the next paragraph. See Also Appendix A where the theoretical transverse momentum and angular resolution of the central and forward tracking systems are discussed.

Central Jet Chambers

The central region of H1 is covered by two concentric multiwire jet chambers (CJC-1 and CJC-2). Charged particles traversing the gas volume of the chambers create secondary electrons and ions. The electrons drift along the electrical field lines and are amplified in a charge avalanche in the strong field near the sense wires.

The wires of the CJC are strung parallel to the z axis. The drifting electrons carry precise information about the r-φ position of the traversing particle. This information is used to

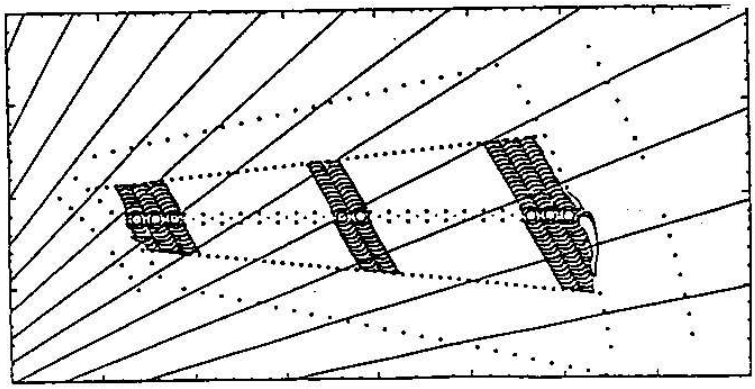

Figure 2.2.: Simulation of a CJC cell indicating the drift regions of the senses wires, drift lines and isochrones. The straight lines represent infinite momentum tracks from the beam axis. Taken from [20].

accurately determine the curvature κ of the particle tracks, which is caused by a homogeneous magnetic field in z direction. The momentum of the particle is proportional to the inverse of κ.

The z coordinate is determined by a simultaneous measurement of the deposited charge at both wire ends. The assumption of a uniform resistivity of the sense wire allows to determine the track position by charge division. As this method only provides moderate resolution the z measurement is supplemented by the information from the central outer z-chamber (COZ). The COZ is located between CJC-1 an CJC-2. The sense wires of the COZ are strung *perpendicular* to the z direction, providing a resolution of $\sigma_z \approx 350\mu$m

A $r-\varphi$ view of the chamber is given in figure 3.2. The chamber is radially divided into cells containing a plane of sense wires in their center, compare figure 2.2. The sense wires are staggered by $\pm 430\mu$m [26] with respect to the wire plane. The cells are limited by field forming wires. Between the sense wires two additional field forming wires are situated, reducing significantly the cross talk between the sense wires.

The cells are *tilted* by the approximate Lorentz angle[3] of 30° with respect to the radial direction. This leads to a field geometry in which the electrons drift perpendicular to high p_t tracks, ensuring optimal resolution for small curvatures (=high p_t). The tilt also has another effect: As it is a priori not possible to decide from which side of the cell the electrons reach the sense wires, a *left right ambiguity* of the hit information evolves. The mirror images of segments of measured tracks are pointing in a much different direction than the original segments because of the cell tilt. In this way most of the ambiguities can be resolved. Finally, most of the tracks cross a tilted sense wire plane allowing to precisely determine the passing time of particles, and thus their bunch crossing of origin.

The approximate drift speed with is 5mm per bunch crossing (=990/CJC-FADC count), the maximum drift length for the outer cells of CJC-1 is 45 mm. The maximal drift time is therefore ~ 9 bunch crossings.

2.2.4. Track Parameters

A track is described by a circle in the r-φ plane transverse to the magnetic field, compare figure 2.3. The curvature κ is the inverse radius of the circle. It is releated to the transverse momentum

[3]The Lorentz angle is the angle between the electric field and the drift direction of the electrons in presence of the magnetic field.

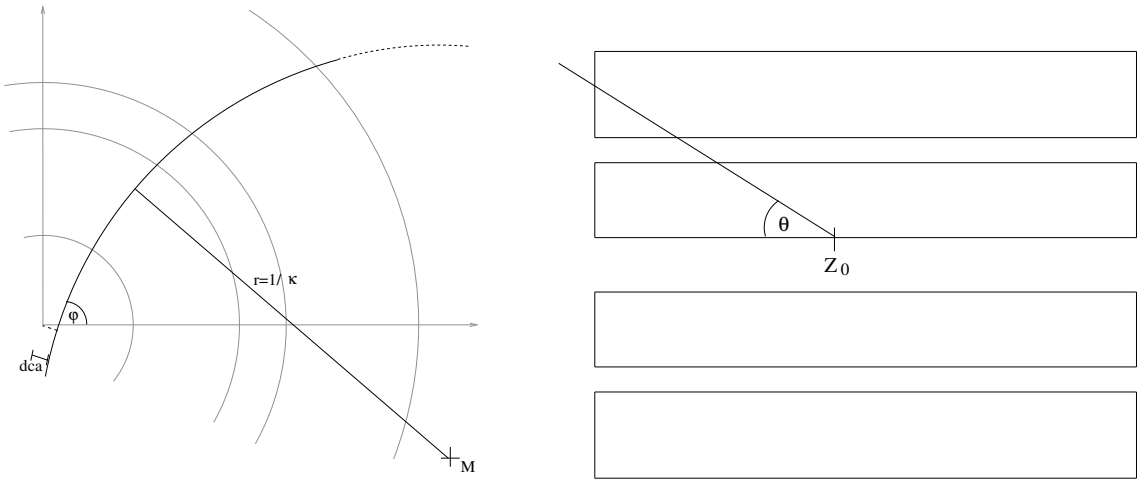

Figure 2.3.: Illuatration of the Track Parameters.

of the particle according to the following equation:

$$p_t \left[\frac{\text{GeV}}{c}\right] = 0.3 \cdot B\,[\text{T}] \cdot \frac{1}{\kappa}\,[\text{m}]$$

- The distance of closest approach (d_{ca}) is the distance between the track and the point of origin.
- The angle φ is measured between the direction of the track at the point of closest approach and the x axis.
- The angle θ is measured between the track and the z axis.
- Z_0 is the z coordinate at the point of closest approach.

The spatial information extracted from the drift time information of the CJC sense wires depends on the assumed passing time $T_{0,\text{track}}$ of the particle. For tracks crossing several cell boundaries $T_{0,\text{track}}$ is determined in a fit during the CJC reconstruction. The bunch crossing of origin of the track is identified using the measured $T_{0,\text{track}}$. The average of all track passing times defines the event CJC-T_0. It's precision is 0.5 ns [20]. The major fraction of tracks caused by cosmic muons can be identified by their deviating T_0.

2.3. The H1 Trigger System

2.3.1. Introduction and requirements

The readout of the H1 detector comprises $\sim$ 270.000 readout channels. In order to cope with the generated amount of data the information from the ADCs is only read out and evaluated for short time intervals. The length of the interval allows for the reconstruction of the detector status at a given time, when the *event* has taken place. The trigger system has to recognize interesting ep events and to initiate the readout.

The basis for this decision is an additional, coarser segmented and fast output of all major subsystems. It is supplemented by information from dedicated fast detector components. The trigger is an hierarchical system consisting of increasingly complex and time consuming *trigger*

Table 2.3.: Rates determining the requirements for the trigger system [27].

process		rate
bunch crossing rate		10.4 MHz
beam induced background	$\lesssim$	50 kHz
ep interactions	$\sim$	1000 Hz
DIS $1\text{GeV}^2 < Q^2 < 10\text{GeV}^2$	$\sim$	40 Hz
DIS $Q^2 > 10\text{GeV}^2$	$\sim$	4 Hz
heavy quark production	$\sim$	0.05 Hz
charged current	$\sim$	0.01 Hz
$D^* \to K\pi\pi$	$\mathcal{O}($	$1000) \cdot \text{year}^{-1}$
DIS at highest Q^2	$\mathcal{O}($	$1) \cdot \text{year}^{-1}$

levels. Each level evaluates only detector signatures that were accepted as potentially interesting by the preceding levels. A positive trigger decision may be falsely initiated by signatures originating from all kinds of *backgrounds*. These have to be identified and rejected. The main background contributions are particles hitting the detector, that are created by:

- interactions of the beam particles with rest gas in the beam pipe,
- interactions of particles diffusing out of the beam into the beam pipe,
- synchrotron radiation emitted by the electron beam and
- muons originating from cosmic radiation.

The beam induced backgrounds are primarily caused by the proton beam, and depend strongly on the conditions of the vacuum and the beam optic. The rates of the main background processes and some exemplary physics interactions are given in table 2.3. The number stated for the beam induced background is an upper limit given by the acceptable current[4] in the tracking chambers and the tolerable radiation dose on the silicon track detectors. (See also subsection 2.3.3.)

2.3.2. The H1 trigger levels

An overview over the trigger levels is given in figure 2.4. The latency of each trigger level is shown on a logarithmic scale. The event pipeline and its interactions with the different trigger levels are depicted in the lower part of the figure. The numbers on the very bottom are the input rate of each trigger level.

Level 1 The latency of the first trigger level (L1) is determined by the signal formation time in the slow detector components (LAr) and the cable delays. It is a multiple of a bunch crossing period, necessitating a buffering of the readout data in so called pipelines in the meanwhile.

Each sub-detector providing L1 trigger signals evaluates independently whether a valid signature was measured for the bunch crossing of concern. All pieces of information (*trigger elements*) are sent to the central trigger and combined to up to 128 *L1-subtriggers* using basic logical operations.

[4]Limited by aging effects at higher currents.

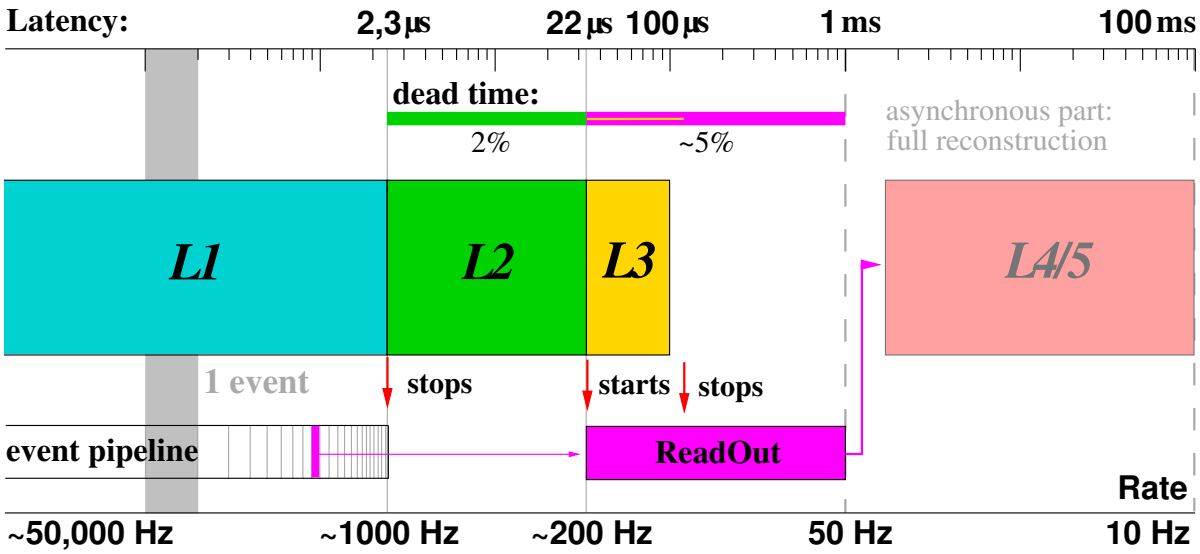

Figure 2.4.: H1 trigger system

The high background rates (see table 2.3) require effective rejection measures to be taken already on L1. Veto triggers fed by information from the time of flight (TOF) system and z-vertex measurements are the most important rejection mechanisms.

At the time the L1 central trigger logic comes to a positive trigger decision the exact bunch crossing of the ep interaction has to be known. This is essential for the correct readout from the front end pipelines. For slow sub-detectors like the LAr calorimeter whose trigger signals may extend over several BCs a valid timing is secured by combination with so called T_0 bits. T_0 trigger bits are extracted from information of sub-detectors with intrinsically good timing resolution, like for example the SpaCal (subsection 2.2.1 on page 10) or the CIP.

Level 2 As the front end pipelines are halted, dead time [28] is being accumulated during the L2 decision. This limits the L2 input rate to $\sim$ 1000Hz, corresponding to a contribution of 2% to the dead time, given the 20μs L2 latency. All L1 raw trigger data of the independent subsystems is provided to L2. Two distinct systems are operating in parallel to achieve the L2 decision. The topological trigger (L2TT) searches for spatial correlations in the L1 trigger signals, using a 16x16 binned representation of the detector in θ- φ space. The second system is the L2 neuronal network (L2NN). It is trained to distinguish background and physics events with previously recorded data.

Each of the systems provides up to 16 *L2 trigger elements* to the central trigger logic. The *L2 subtriggers*, being logical combinations of the L2 trigger elements, are validated representations of the L1 subtriggers. This association is necessary for the trigger efficiencies to be well defined [29].

In case of a *L2Keep*, the readout of the detector is started. In contrast, a *L2Reject* resumes the front end pipelining, that was halted by the L1Keep.

Level 3 The full detector readout initiated by the L2Keep signal, takes roughly $\sim$1 ms. This limits the possible readout frequency to about 50Hz (5% dead time contribution). The third trigger level is designed to stop the readout for identified background events within 100 μs and thus allowing for a higher L2Keep rate.

A former implementation of the L3 System using AM RISC 29000 processors was only used in test operation, because it did not meet the requirements of the algorithms in terms of computing power. In the context of the FTT a new L3 system using a farm of PowerPC CPU boards will be put into operation. Studies have shown, that a L3 latency of 100 μs is suitable for efficient processing of trigger algorithms, while allowing for a L3 input rate of $\mathcal{O}(100)$.

Level 4/5 [5] After the readout out has finished the detector pipelines are restarted and the event data is passed to a processor farm. Because the detector operation is resumed during the fourth trigger level, it is called asynchronous and does not contribute to the dead time.

The L4/5 decision is based on a full reconstruction of the event only lacking the final calibration constants. It reduces the detector output from a rate of 50Hz down to roughly 10Hz written to tape.

2.3.3. HERA-II Selective Trigger Strategy

As the rates stated in table 2.3 indicate, it is not possible to readout and store all *ep* interaction events. Therefore a selection of interesting physics events has to be performed already on trigger level (*selective* trigger). If the rate reduction of the first three trigger level is not sufficient, events have to be discarded in order to avoid an unacceptable dead time fraction. This is implemented by introducing so called *prescale factors [30].*

As already mentioned in subsection 2.1.1, the physics program of H1 after the upgrade is concentrating on low cross section processes. Among those are high Q^2 events which have a clear experimental signature caused by the scattered electron detected in the SpaCal or LAr. They can be triggered with the existing H1 trigger system. The identification of specific final states in low Q^2 events as needed for exclusive and semi inclusive analyses is quite challenging on the other hand. Amongst other measures the jet- and fast track trigger systems are intended to cope with this task. They deliver additional information about the hadronic final state of the reaction.

[5] The name L4/5 for arises for historical reasons.

3. Fast Track Trigger

As mentioned the HERA I trigger strategy was mostly relying on the detection of the electron in the LAr or SpaCal calorimeter. Most ep interaction events however involve very low four momentum transfers at which the electron escapes through the beam pipe and cannot be measured (photoproduction events). Interesting final states like vector mesons or e.g. D^* events hidden in photoproduction can only be triggered with adequate efficiency when taking into account additional (track) information. The FTT delivers this information with high precision allowing for the reconstruction of the invariant masses of decay particles already on trigger level. In simulations it was shown, that the FTT reaches for example an efficiency of 80% to 90% in the selection of D^* candidates at rate reductions of a few tens relative to the HERA-I trigger setup [31].

3.1. Features

The Fast Track Trigger (FTT) System is providing track based information to the first three trigger levels of H1 and thus implementing the third level for the first time. It is replacing the so called DCRΦ trigger [32, 33], which was delivering CJC based information to L1 and L2 trigger systems in a relatively coarse manner in the past.

The FTT *L1* trigger information is provided basically in form of track multiplicities for different p_t thresholds and of track topologies based on the φ distribution of the tracks; the lowest p_t threshold is 100 MeV, compare table 3.1. The minimal p_t threshold of the old DCRΦ trigger used to be 400 MeV.

During the latency of the second trigger level a three dimensional track reconstruction of up to 48 tracks[1] is performed. The information for *L2* is composed similar to the L1 information, comprising p_t ranges, p_t sums, charge sums and topologies in the r-φ plane, but available with higher precision, compare table 3.2. It should also be possible to calculate and cut on the invariant mass of two prong vector meson decays.

The *L3* trigger decision is accomplished by a farm of CPU boards. Physics working group defined algorithms are able to calculate and cut on invariant masses of multiparticle decays. The decision is based on the tracks reconstructed during the L2 phase, which can be combined with the L2 trigger information from other subsystems (PQZP data). The precision of the track information employed on L3 is close enough to the full reconstruction to allow for significant background rejection at high trigger efficiencies, compare figure 3.1.

3.2. Wire Layout

The FTT uses information from twelve out of the 56 concentric wire layers of the central tracking chambers (figure 3.2). The wires are grouped into four *trigger layers*, each composed of three CJC layers, the outermost trigger layer being located in the outer CJC-2. The trigger layers are divided into 30 (CJC-1) or 60 (CJC-2) *trigger cells* according to the partitioning of the jet chambers. Altogether the FTT comprises 150 cells, each containing three wires. Cells are the

[1] According to simulations the number of 48 tracks is sufficient for 95% of all ep events of interest.

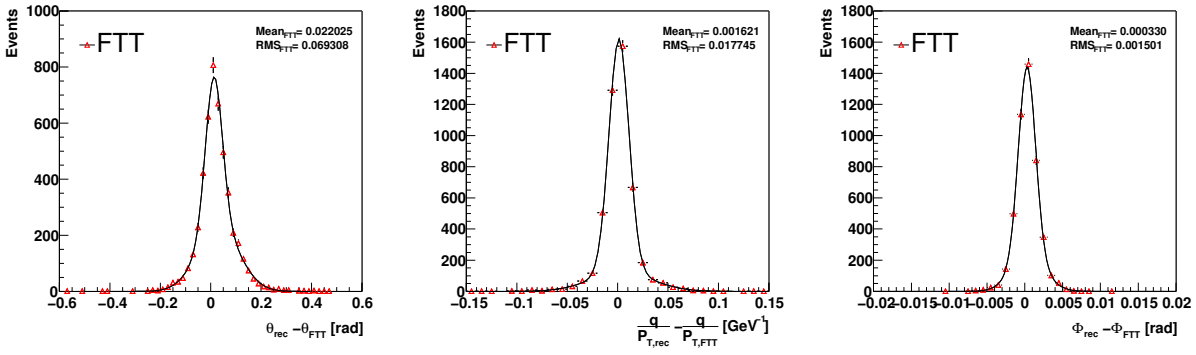

Figure 3.1.: L2 resolution of the parameters Θ, $1/p_t$ and φ of the FTT reconstructed tracks relative to tracks of the full reconstruction are shown for a simulated $J/\Psi \rightarrow \mu^+\mu^-$ sample [34].

Table 3.1.: FTT L1 trigger elements as implemented 02-2005. The highest possible number of tracks above a certain p_t threshold always means e.g. 7 *or more* tracks found.

trigger bits	description	name
104	T_0	FTT_T0
105-107	number of tracks with $p_t >$ 100MeV	FTT_mul_Ta
108-109	number of tracks with $p_t >$ 160MeV	FTT_mul_Tb
110-111	number of tracks with $p_t >$ 400MeV	FTT_mul_Tc
136	any FTT segment found	FTT_seg
137-139	charge sum	FTT_Qtot
140-141	number of tracks with $p_t >$ 900MeV	FTT_mul_Td
142-143	number of tracks with $p_t >$ 1800MeV	FTT_mul_Te
144-151	φ topologies	FTT_topo_[0-7]

smallest unit of the FTT where the track segment finding is performed (section 3.3). Tracks having certain combinations of charge and curvature tend to cross cell boundaries within a trigger layer. Therefore hits on the inner right and outer left sense wires of neighbouring cells are taken into account during the segment finding. The thereby composed subunit is call *trigger group*.

3.3. Reconstruction Algorithm

The reconstruction algorithm of the FTT is divided into track *finding* based on pattern recognition (segments) and track *fitting* that is performed with the associated hits afterwards. The implementation is very efficient allowing the first track identification already $\sim 1.3\,\mu$s after the end of the maximum drift time.

The *segment* finding is performed using the r-φ (=drift time) information of the jet chamber (see section 3.6). For reasons of efficiency it is performed in the static partitions given by *trigger groups*. The hits of a track are measured in a single trigger group per trigger layer. The hit patterns of each trigger group are compared to precalculated masks, to identify valid track segments.

The track parameters κ and φ are extracted from the segment under the assumption of a

Table 3.2.: Possible trigger elements for FTT - L2.

trigger bits	description
0-2	number of tracks with $p_t >$ 100MeV
3-4	number of tracks with $p_t >$ 400MeV
5-6	number of tracks with $p_t >$ 900MeV
7-8	number of tracks with $p_t >$ 900MeV
9-10	number of tracks with $p_t >$ 2GeV
11-12	number of tracks with $p_t >$ 5GeV
13-15	total charge
16-19	back to back topologies
20-23	jet topologies
24-25	threshold of track with highest p_{t}
26-27	threshold for $\sum \lvert p_t \rvert$
29-31	vector mesons

track originating from the vertex. They are measured sufficiently precisely, to join compatible segments to tracks (*linking*). At least two out of four possible matching segments from different layers define a valid track.

The L1 trigger decision is based on the linked r-φ tracks. In case of an event accepted by the L1 trigger logic the track segments are *refined* and *validated* during the L2 phase. For this purpose more precise r-φ hit information than available on L1 is used (see also B.1) and the *linking* is repeated. Two fits are performed to obtain the final L2 track parameters. In the r-φ plane one effective data point per track segment plus the position of the run Vertex is fitted using a Karimäki circle fit [35]. The z information of each hit is fitted with a least squares straight line fit in the s - z plane, where s measures the arc length of the track. Both fits are computed in a non-iterative way. Their implementation is described in detail in [27].

3.4. Implementation

The first two trigger levels are implemented using custom designed electronic boards equipped with FPGAs and DSPs. The fast data connections between the different boards are realized using the LVDS bus. (compare Appendix B.3 for a brief explanation of these technologies). They are summarized in figure 3.3: The analogue signal are digitized on the 30 front end modules, where the segment finding is realised. The segment data streams are merged on the five mergers and sent to the linkers. The L1 linker obtains the trigger decision which is passed to the central trigger logic. The L2 linker passes the linked tracks to the fitter chain, which is completed by the L2 decider. From here the fitted tracks are sent out to the L3 system. The third trigger level uses commercially available PowerPCs CPU boards to process the selection algorithms. They are supplied with track data using the FPDP bus. The *receiver card* provides the conversion of LVDS data stream into the FPDP protocol.

The hardware is housed in altogether six electronic crates. Each crate is controlled by a CPU board (crate master) that uses the VME backplane bus to monitor the custom boards. The crate masters are connected to the *FTT master* in the control room via ethernet. The FTT master is a linux pc which is steered by commands from one or more FTT graphical user interfaces (GUI). Also the readout of persistent data is handled by the crate master PowerPCs.

The different hardware modules of the FTT are introduced in the next paragraphs. A detailed

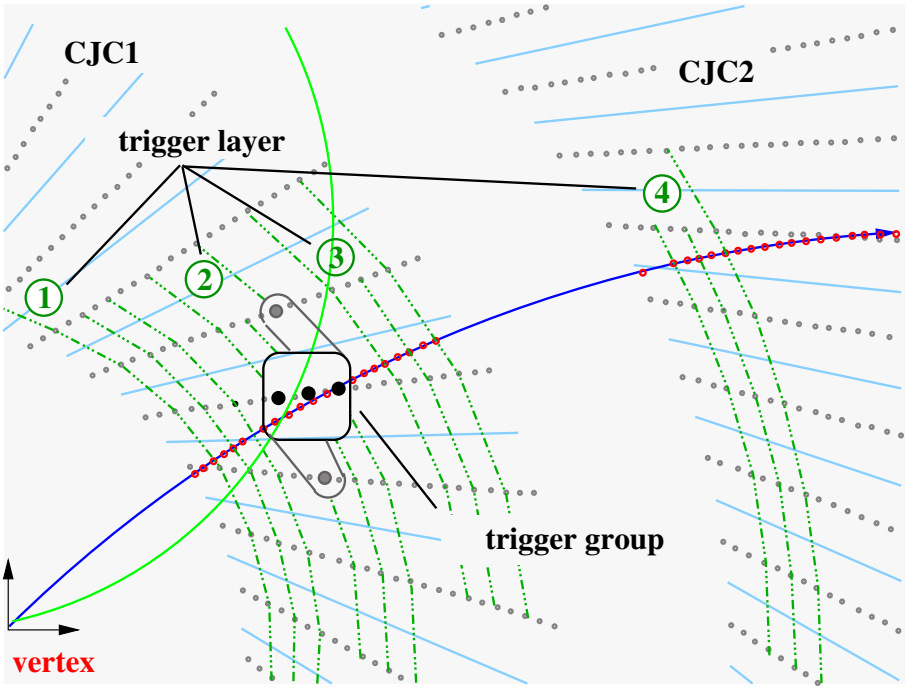

Figure 3.2.: The wire layout of the FTT. The green low momentum track is crossing the cell boundary, but is contained in the trigger *group*

description of the data processing especially on the front end modules is given in Appendix B.

Buffer Cards The buffer cards are connected to the analogue output of the central tracking chamber FADC cards. They contain the electronics needed to provide the old DCRΦ trigger and the FTT with input signals at the same time.

Front End Modules One front end module (FEM) processes the analogue signals from five adjacent trigger cells. The tasks of the FEMs are divided into two operating modes: L1 and L2 mode. In L1 mode the analogue input is digitized and hits are identified by the qt algorithm. The drift time information is stored in shift registers in order to produce characteristic hit patterns. These are compared to precalculated patterns (calls *masks*) and valid track segments are identified. For reasons of performance this comparison is performed with a low granularity version of the shift registers, during L1 mode. The κ-φ information of accepted segments is sent out to the merger. During L2 mode information from the full granularity of the shift registers is used to get *refined* track segments. Also the L2 segments are transmitted to the merger.

Multi Purpose Boards All other processing modules of the L1 and L2 system are variants of the FTT multi purpose board (MPB): the merger, the linker, the fitter and the L2 decider. The MPBs contain two FPGAs and optionally four DSPs (fitter). They can be equipped with up to four piggy-back add-on cards that provide the LVDS connections to the other modules. There are piggy-back cards with two input ports (i/i) and cards with an input and an output port (i/o) [36].

Merger Because the MPB can only be equipped with a limited number of LVDS input channels it is not possible to connect all FEMs to the linkers. Instead the data streams of six FEMs is combined into one stream by the merger module. There are in total five merger cards,

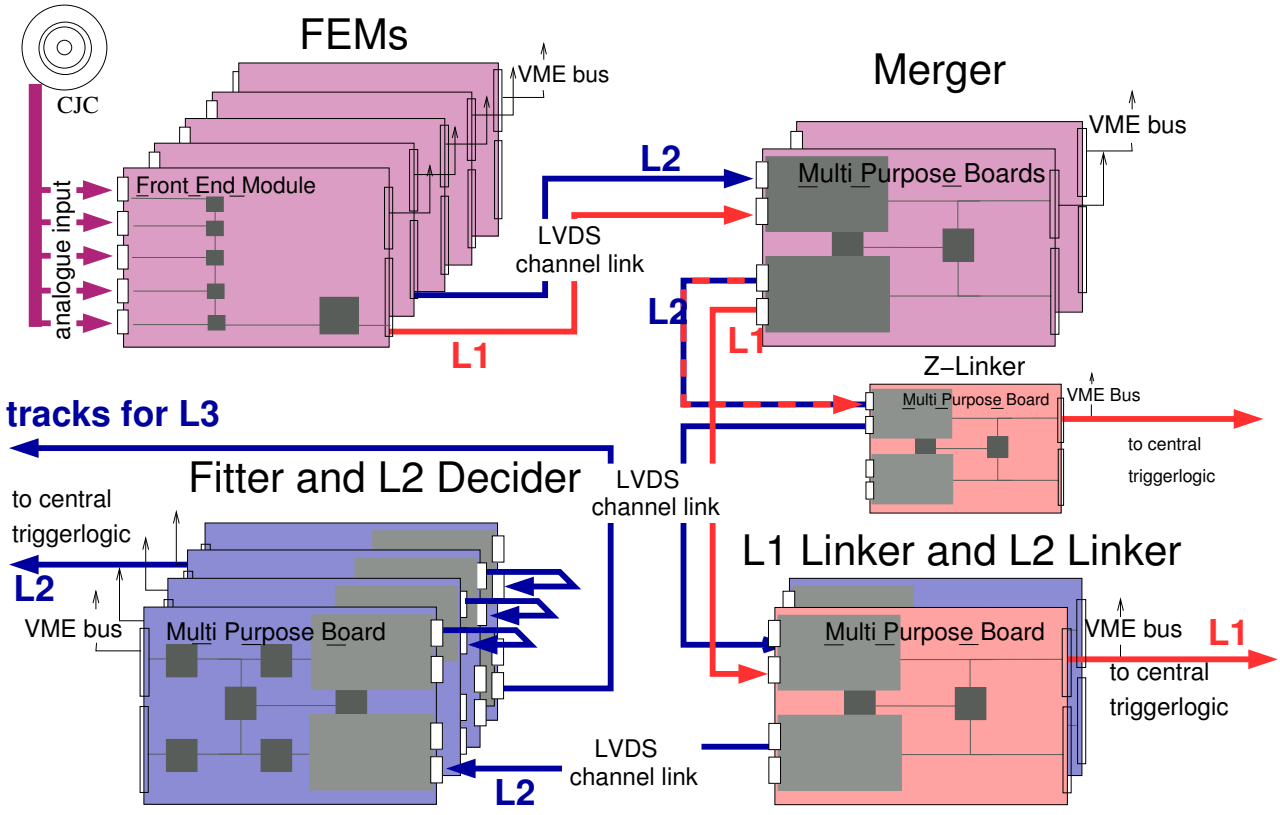

Figure 3.3.: Hardware and LVDS connections of the FTT level one and two system.

one for each trigger layer of CJC-1 and two for the fourth trigger layer in CJC-2. The mergers send all segments to the respective (L1/L2) linker card [37].

Linker The L1 and L2 linker are composed of the same hardware. Also the algorithm is in principle identical for both trigger levels. The difference lies only in the precision of the input data. The segments are written into a two dimensional κ-φ histogram. If at least two segments lie in the same area of the histogram to some precision they are connected to a track. The linking algorithm is described in detail in [31]. The L1 linker also obtains the trigger decision by counting valid tracks and comparing to valid trigger topologies. The L2 linker sends the linked track segments to the fitter cards.

Fitter The fitter cards are connected by a chain of channel links. On each of the four DSPs of the fitter up to two tracks are fitted while remaining track segments are passed on to the next fitter. The track parameters are obtained by a fit in the r-φ and one in the r-z plane. In figure 3.1 the FTT track parameters obtained in simulations are compared to the result of the full offline reconstruction. The fitter is described in [27]. The fitted tracks are transmitted to the L2 decider.

L2 Decider On the L2 decider the trigger decision is obtained and the tracks are passed on to the L3 system. The L2 trigger elements are listed in table 3.2 on page 19. The FPGA and the four DSPs are available for the evaluation of the recognized tracks [38].

Receiver Card In order to provide fast data distribution to the up to 16 CPU boards of the L3 system a point to multi-point bus protocol is used (FPDP). The receiver cards provides

the conversion of the LVDS point to point data connection to the FPDP bus [31].

PowerPC CPU Cards The L3 system uses up to 16 commercially available CPU boards with VME backplane bus. On each board a different selection algorithm is processed. During the specification of the system boards equipped with a 450MHz G3 PowerPCs where tested to provide the necessary processing power for L3. Nowadays faster CPUs provide the possibility to improve the L3 performance. [39]

3.5. Qt Algorithm

In a drift chamber an ionizing particle is detected as a pulse in the current measured at both ends of a sense wire. The fraction of the charge measured on each wire end allows to determine the z coordinate of the hit. The Qt algorithm identifies pulses and measures the charge by integrating over the current as a function of time.

The algorithm used for the FTT facilitates the difference of samples[2] (dos) technique for the pulse identification. The algorithm examines the sum of the samples of both wire ends. The difference between each two consecutive added samples is computed and compared to a threshold. A hit is accepted when the threshold is exceeded and the difference is negative or zero for at least three digitization steps after the maximal dos. The time of the hit complies with the sample with the maximal dos.

If a hit is identified the charge integration is performed for each wire end separately. The samples of a certain time window around the hit are added up. Afterwards a pedestal subtraction is done in order to take into account the different no-signal current of the wires. The pedestal is summed up in a time window a few samples before the hit. When a *sequence* of hits is found the pedestal is only recomputed when the hits are sufficiently separated. Otherwise the pedestal of the first hit is reused for the subtraction from the second and following hits.

In the context of this thesis a graphical display for the FTT Qt algorithm was written (section 4.2).

3.6. Segment Finding

The segment finding is performed in the r-φ plane of the CJC. It is illustrated in figure 3.4. An ionizing particle traverses the chamber volume and leaves a track of secondary electrons. In the strong electrical field of the chamber these electrons drift towards the sense wires. When a hit is measured on a FTT wire an entry is made in the corresponding shift register. As time evolves the register entry is shifted just like the electrons drift. At the end of the maximal drift time a pattern corresponding to the track is contained in the shift registers. This pattern is compared to a set of precalculated masks each mask representing a valid track segment. If a compatible mask is found the track parameters κ and φ are extracted from the mask number.

[2] A sample is the value of a digitized quantity at a given clock cycle.

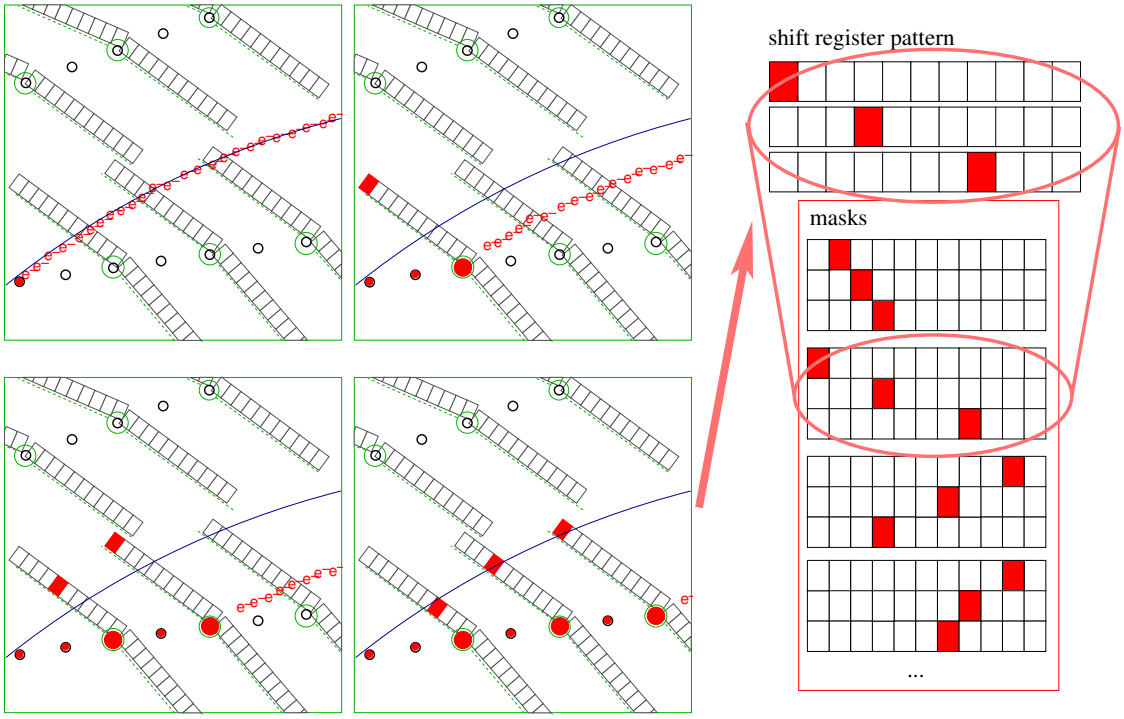

Figure 3.4.: Segment finding: the information in the shift registers is illustrated together with the r-φ view of the CJC for different points in time. After the maximal drift time the registers match a precaculated mask, compare section 3.6.

4. Data Quality of the FTT

As described above the FTT is composed of several hardware modules. On each module some programmable logical component realizes a step of the data processing. In order to be able to debug and monitor the behaviour of the 'FTT software' data can be read out from various modules. It is passed to the standard readout chain and stored together with the information of the H1 subdetectors. In the context of this thesis tools were developed to handle and analyse parts of the FTT monitoring data in an object oriented framework.

The precision of the FTT track reconstruction is comparable to the one of the full offline track reconstruction (compare figure 3.1). For this reason similar efforts have to be put into the precise calibration of the input data. The approaches for the r-φ and z calibration discussed below are oriented on the CJC calibration procedures implemented in `h1rec`, the official reconstruction programme.

4.1. Technical Framework

The detector readout is stored in a simple binary data format that was designed for convenient use with FORTRAN and is called FPACK. The FPACK files contain so called BOS banks, building up a structure of well defined pieces of information. Special libraries are used to read data from FPACK files into memory, where the banks are available in the so called BOS common. The H1 OO[1] software facilitates these libraries to convert a subset of the detector readout banks into objects that can be handled by the ROOT[2] object input/output system.

The fttroot2 framework is however not based on H1 OO. It uses the BOS and FPACK libraries to read the raw data files directly. This choice was made

- to be able to have a quick and intuitive way to view the content of a given raw data file.
- because of the necessity to perform the conversion of raw data files into ROOT objects as distinct time consuming work step in H1 OO.
- because H1 OO is not designed for the needs of a raw data analysis using data structures which are still under development.

The program fttroot2 provides C++ classes allowing the convenient access to BOS banks (module H1BankMan and H1FttBos). 'Data objects' are created on-the-fly and only on demand (FttCommon) using the bank access classes. All this functionality is available in an interactive ROOT shell. A graphical front end is provided for basic features like opening raw data files and showing their bank content.

[1] H1 OO is the new data storage and analysis environment of the H1 experiment and is based on ROOT.
[2] ROOT is an object oriented analysis framework, http://root.cern.ch.

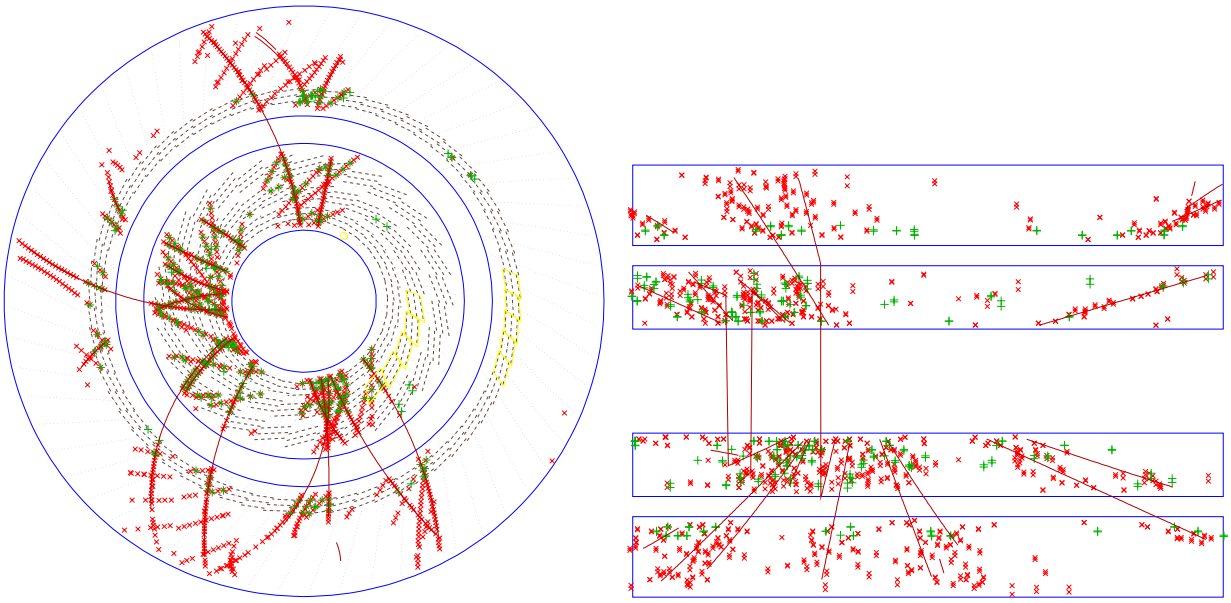

Figure 4.1.: FTT display contained in fttroot2. The r-φ view (left) and r-z view (right) of the chamber are available. FTT hits (green) and hits found by the standard CJC readout (red) are shown together with the tracks of the offline reconstruction. The yellow boxes are cells of which the digitized sense wire current (raw data) was read out.

4.2. Graphical FTT Display

A graphical display for the FTT input data was implemented in order to provide an first overview. The side (r-z) and frontal (r-φ) view of the central tracking chamber of H1 are displayed, compare figure 4.1. Special effort was put into the visualisation of the Qt algorithm running on the front end modules of the FTT. The two displays are connected, such that the Qt information of interesting cells identified in the CJC view can be directly selected for the Qt display. A qualitative understanding can be gained by interactively varying the parameters of the Qt algorithm, compare figure 4.2.The parameters which can be varied are:

- the length of the time window for the integration (Depth)
- the offset between the pedestal time window and the hit time (PedDelay)
- the difference between the pedestal and the pulse integration time window (TimeDelay)
- the number of samples for which the pedestal is frozen after the hit (VetoDepth)
- the threshold for the added dos of both wire ends (Threshold)

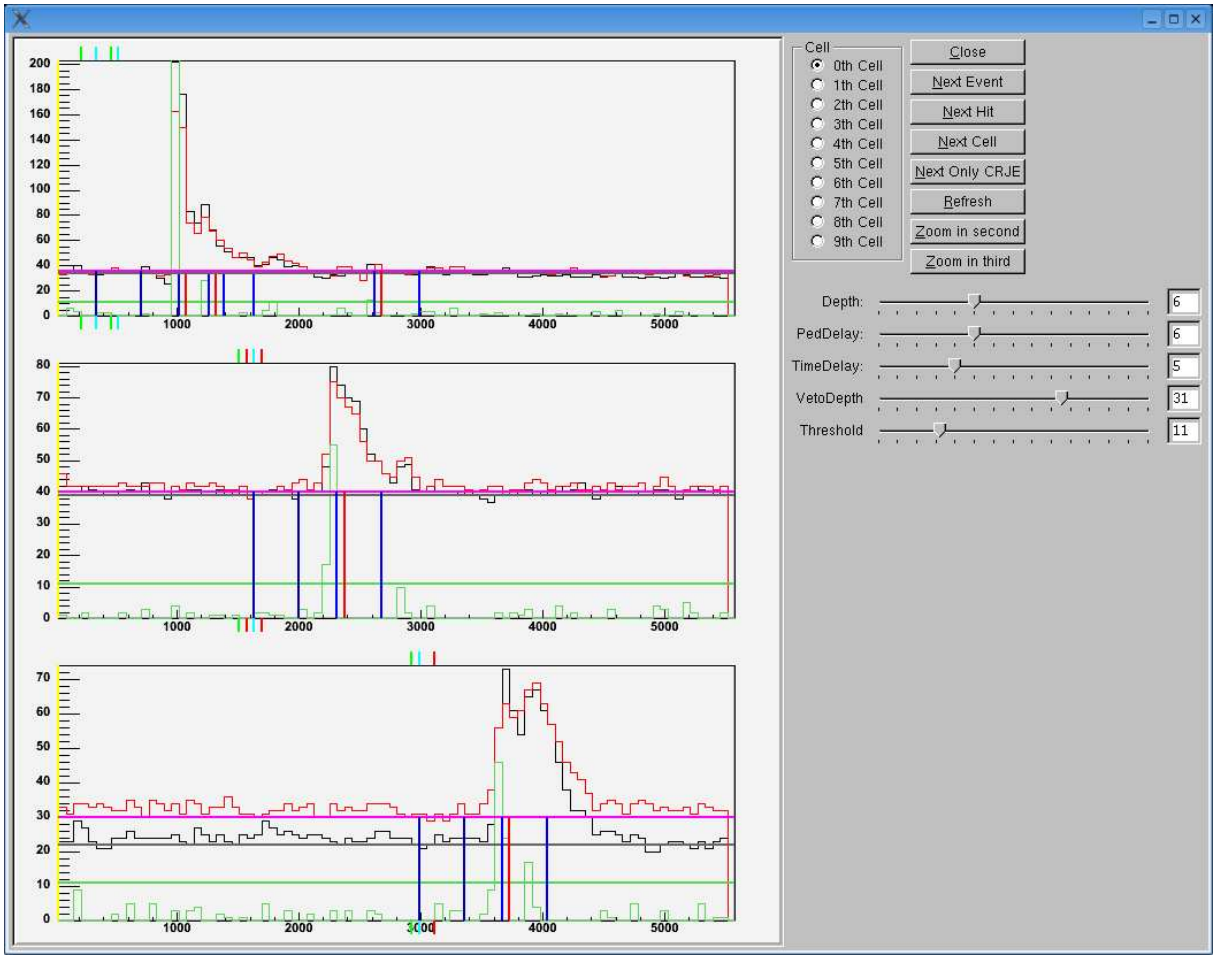

Figure 4.2.: Qt algorithm display. The algorithm is described in subsection 3.5. The current measured at the positive (red) and negative (black) end of the sense wire is displayed as function of time. Time is shown in units of CJC FADC counts ($\hat{=}10\mu$m). The green histogram is the added difference between each two consecutive samples (=bins). A hit is found when the difference of samples (dos) exceeds a given threshold, which is shown as green horizontal line. The time at which the hit is found is displayed as red vertical line. The pedestal is integrated between the first pair of blue lines while the hit charge is integrated between the second pair. The result of the pedestal integration is shown for the positive (magenta horizontal) and negative (grey horizontal) wire end. The parameters of the algorithm can be varied interactively by moving the sliders on the right of the window. See text for an explanation of the parameters.

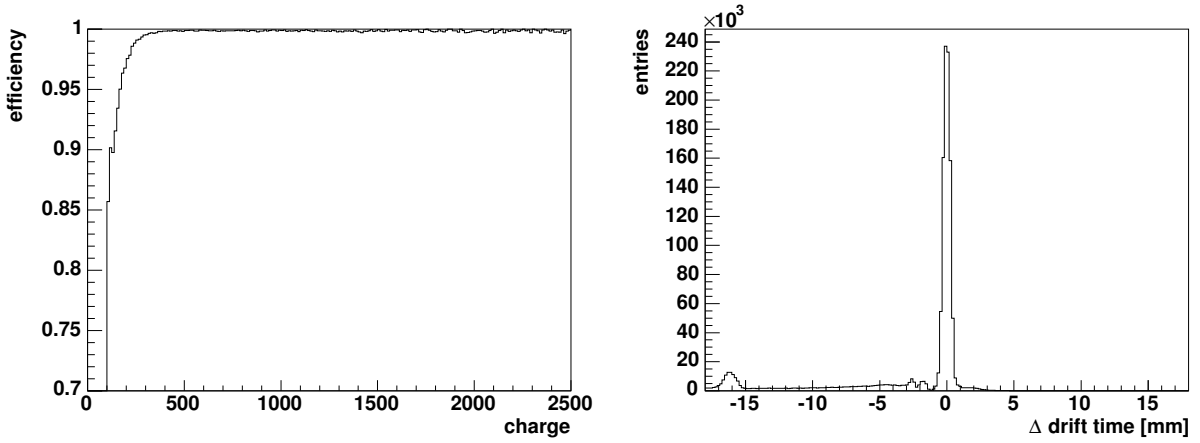

Figure 4.3.: The fraction of CJC wires at which at least one hit is found by the standard readout and also by the FTT is shown as function of charge (arbitray units, see subsection 4.3.1). On the right the difference in drift time of a FTT hit and the corresponding CJC hit is shown.

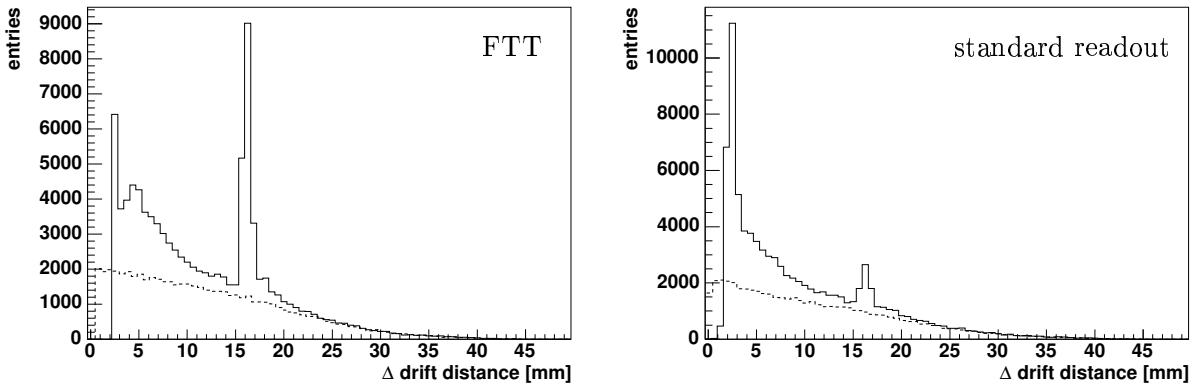

Figure 4.4.: The drift time minus the drift time of the first hit on the wire is shown for all hits. The graph on the left shows FTT hits, while the one on the right hand side shows the hits of the standard readout. The dashed lines display the difference between the first hit and a randomly chosen hit on the same wire, thus showing the expected form of the spectrum for uncorrelated hits.

4.3. Hit Finding Efficiency

The hit finding efficiency is measured for each FTT wire and as a function of charge in order to monitor the input data of the FTT. The single hit efficiency is of interest for the optimization of the Qt algorithm and to check the correct functioning of the FTT front end electronics. The results of different methods of efficiency determination are shown and compared using a data sample taken during *ep* interaction running at the beginning of 2005. The hit efficiency can be obtained

- by comparison to the hits found by the standard readout of the CJC.
- using the ratio of hit tripletts and doubletts in a FTT cell.
- by comparison to hits recalculated from the tracks found by the offline reconstruction.

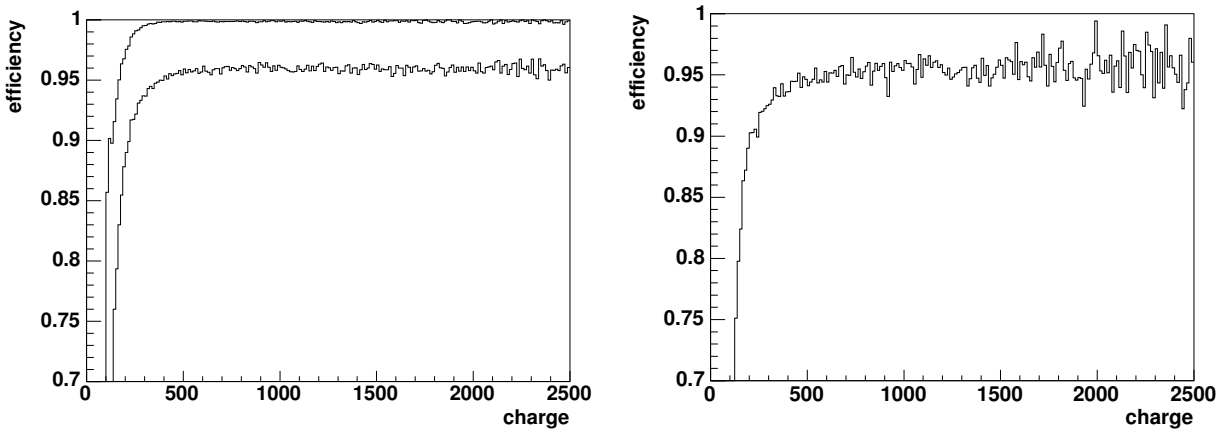

Figure 4.5.: On the left the efficiencies obtained by comparison with the standard CJC readout are shown. The lower efficiency is gained when requiring a coinciding drift time. The right plot shows the efficiency gained from the number of hit doubletts and tripletts in FTT cells as a function of charge.

4.3.1. Comparison with Standard Readout

The FTT extends the existing F1001 readout of the central tracking chambers. The efficiency of both 'independent' systems can be derived by comparison of the results of the readouts. The 'efficiency' of the FTT is shown in figure 4.3 as a function of charge. It should be noted, that the charge distribution of all hits has a maximum between 200-300 units. The units of the measured charge are determined by the digitisation electronics, the FTT charge is a factor of 1.25 smaller than the F1001 charge (which is also the ratio between the F1001 sampling frequency and the FTT sampling frequency).

After Pulses

Also shown is the difference of the drift time of the FTT and the F1001 hit. It can be seen that the majority of hits measured in the different systems have approximately the same drift time. But there is also a flat distribution of hits that don't match in drift time as well as a peak at roughly -16 mm (= 300ns) in the spectrum.

The time spectrum of additional hits on a wire helps to understand this behaviour (figure 4.4). The difference in time between each additional and the first hit on a wire is plotted for all FTT wires. Qualitatively both systems show the same properties: Pulses in the wire current sometimes lead to the detection of two or more hits. The second hit is not found before the end of the first pulse (gap at low differences), but preferably close in time to the primary hit. After a time difference corresponding to 16mm drift distance there is a peak in the hit finding probability. These so called after pulses are caused by reflections in the analogue electronics. They have a much smaller pulse height than the primary pulse. The FTT system detects after pulses more often than the standard readout. This is due to a lower pulse threshold chosen to optimize the hit finding efficiency at the cost of an increased probability to find noise hits. Noise hits are not critical for the FTT because hits not matching to valid track segments are not taken into account by the reconstruction algorithm.

Drift Time Requirement

In order to account for the fact that hits with a deviating outcome of the drift time measurement are missed by the FTT, a matching drift time can be required in the efficiency calculation. The inclusion of too many noise hits is avoided by excluding hits found less than 1 mm after another hit or in the region where reflections are expected ($1.5\text{mm} < T_{\text{reflection}} < 1.75\text{mm}$).

In the left part of figure 4.5 the efficiency with and without a drift time requirement ($|\Delta T| < 1.5\text{mm}$) is shown. The measured efficiency increases with rising charge and saturates at roughly 95%.

4.3.2. Triplett Efficiency

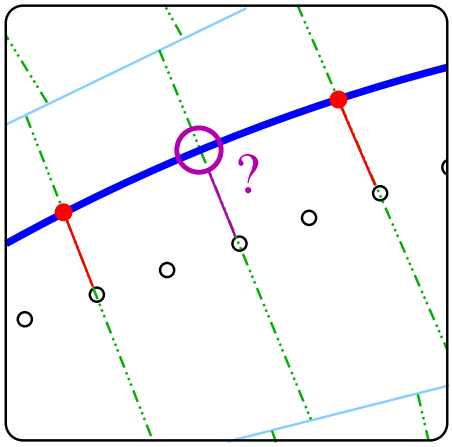

Figure 4.6.: Tracks crossing a FTT cell that deposit hits on the outer wires of the cell also cross the acceptance of the middle wire. Three hits in a FTT cell are called a hit triplett, while hits only on the outer wires are called doublett.

The ratio of hit *tripletts* and hit *doubletts* measured in a FTT cell is an independent measure for the hit finding efficiency. It is assumed that a track that deposits hits on the two outer wires of a cell also traverses the acceptance of the middle wire, see figure 4.6. The number of track segments where the middle hit is found determines the triplett efficiency

$$\epsilon = \frac{N_{\text{triplett}}}{N_{\text{triplett}} + N_{\text{doublett}}}.$$

The right part of figure 4.5 shows the triplett efficiency as a function of the average charge of all hits measured in the cell. It is of similar size as the efficiency obtained in hit-wise comparison when applying the drift time cut.

4.3.3. Comparison with Reconstructed Tracks

Instead of comparing the FTT readout with single hits of the standard readout it is also possible to use the knowledge about particles tracks found by the full offline reconstruction. Hits are recalculated from the track parameters of tracks fulfilling certain quality criteria, compare table 4.1. The fraction of these hits found by the FTT is measured for each FTT wire. In figure 4.7 the difference ΔT between the drift distance of the FTT hits and the recalculated hits is shown. The width of the peak is determined by the strictness of the track quality requirements.

Table 4.1.: track quality requirements as applied for efficiency measurement by comparison with tracks. The cuts are selected to be compatible with cosmic tracks that roughly cross the vertex region, but also high p_t tracks from ep interaction runs.

cut	comment
$(0.003 \cdot 1.15)/\kappa > 0.5$	A minimal transverse momentum is required to suppress multiple scattering between the chambers.
$d_{ca} < 10$cm	cut on distance to vertex
$Z_0 < 60$cm	cut on z at d_{ca}
rStop−rStart > 16cm	A minimal track length is an indication for good tracks.
$30° < \Theta < 150°$	The polar angle is restricted to the FTT acceptance.
$445 < T_0 < 465$	Only cosmics within a time window compatible with lumi tracks are accepted.
$\chi^2 < 1.5$	χ^2 over number of degrees of freedom has to be compatible with expectation.
$d\varphi$<0.01	the parameter error obtained in the fit has to be small.

A cut on $|\Delta T| < 1.5$mm is applied for the efficiency computation. In figure 4.8 the efficiency ϵ_T determined by this method is compared to the one obtained by hit-wise comparison.

Being obtained from the same data sample as the other efficiencies ϵ_T involves less statistics because only a small fraction of the hits is fitted by a track fulfilling the quality criteria. This is the reason for the fluctuations of the obtained efficiency. The overall efficiency is slightly lower than the one of the hit-wise comparison. Also an inefficient cell is identified, which is not visible in the hit-wise comparison.

4.3.4. Results

The efficiencies measured with different independent methods are in agreement to the 10% level. Because of its loose requirements the hit-wise comparison without timing cut is a good first check for the correct functioning of the front end electronics. When requiring a coinciding drift time the method gives a more realistic estimate of the hit finding efficiency. The triplett method has got the advantage of being independent from the standard readout. But it is only able to measure the efficiency of the middle wire of a cell. The comparison to tracks is sensitive to efficiency degradations effecting both systems, because tracks are still found with some missing hits.

4.4. Calibration of the FTT readout

In order to obtain the desired resolution during the track reconstruction both the drift time (r-φ) and the z information measured in the front end electronics have to be calibrated. The calibration procedures exploit a similar approach as the calibration of the standard readout data does. The global models (explanation below) used for the calibration are however different. For the interpretation of the r-φ data an offset in the drift time, the alignment in the r-φ plane and drift velocity and Lorentz angle corrections have to be accounted for. The z determination by charge division requires the effective wire length and z shift to be calibrated.

In the following the general method used for the calibration procedure (*millepede*, see subsection 4.4.4) is introduced. The implementation for the z coordinate which is somewhat simpler

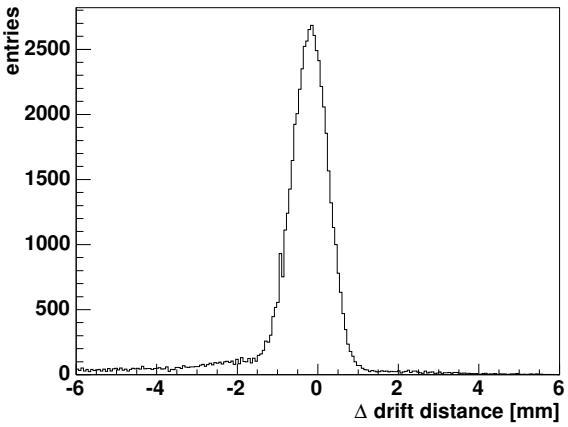

Figure 4.7.: Deviation of FTT hits from reconstructed tracks. The calibration described in section 4.6 was not applied beforehands. It can be seen, that the cut at $|\Delta T| <$ 1.5mm accepts all well matching hits.

than the drift time calibration is explained in detail in order to illustrate the necessary steps. The calculation of the derivatives needed for the z calibration is shown.

4.4.1. Calibration Procedure

A tracking detector measures several space points (*hits*) of the trajectory (*track*) of a traversing charged particle. During the reconstruction a mathematical function describing the track is fitted to the spatial information of the hits. The function usually has about three or four parameters and is called *local model* here. The hit information may be shifted in a systematic way, giving rise to the need for a calibration. This shift may for example be caused by a misalignment of detector components or properties of the analogue electronics, that are not known a priori. The effect of the miscalibration on the hit information is described by a mathematical model using so called *global* or alignment parameters. There may be several hundreds of global parameters depending on the complexity of the tracking device. In a calibration procedure the values of the global parameters have to be extracted from the data. Once the miscalibration is known, the hit information can be corrected in order to get an unbiased track reconstruction.

4.4.2. Extraction of the global parameters

The global parameters have to be determined in a fit to the data. The most intuitive approach is to fit the local models to the uncalibrated data and extract the global parameters from the difference between the local models and the measurements, the *residuals*. This can be repeated in an iterative way: the *first* order corrected data can be refitted and the (first order) corrected residuals can be evaluated in order to get the *second* order correction for the global parameters, and so on. This method defines an iterative fitting procedure for the global parameters. The convergence and the unbiasedness of this procedure are however not granted [40]. A better method is an overall fit (e.g. least squares minimization) of the data of many tracks, each being described by a local model and the influence of the global model, compare figure 4.9. For a two dimensional[3] track fit the sum of least squares is of the form (the formulas used in the actual implementation can be found in [40])

[3] A 3d fitting problem can usually be split into two 2d fits.

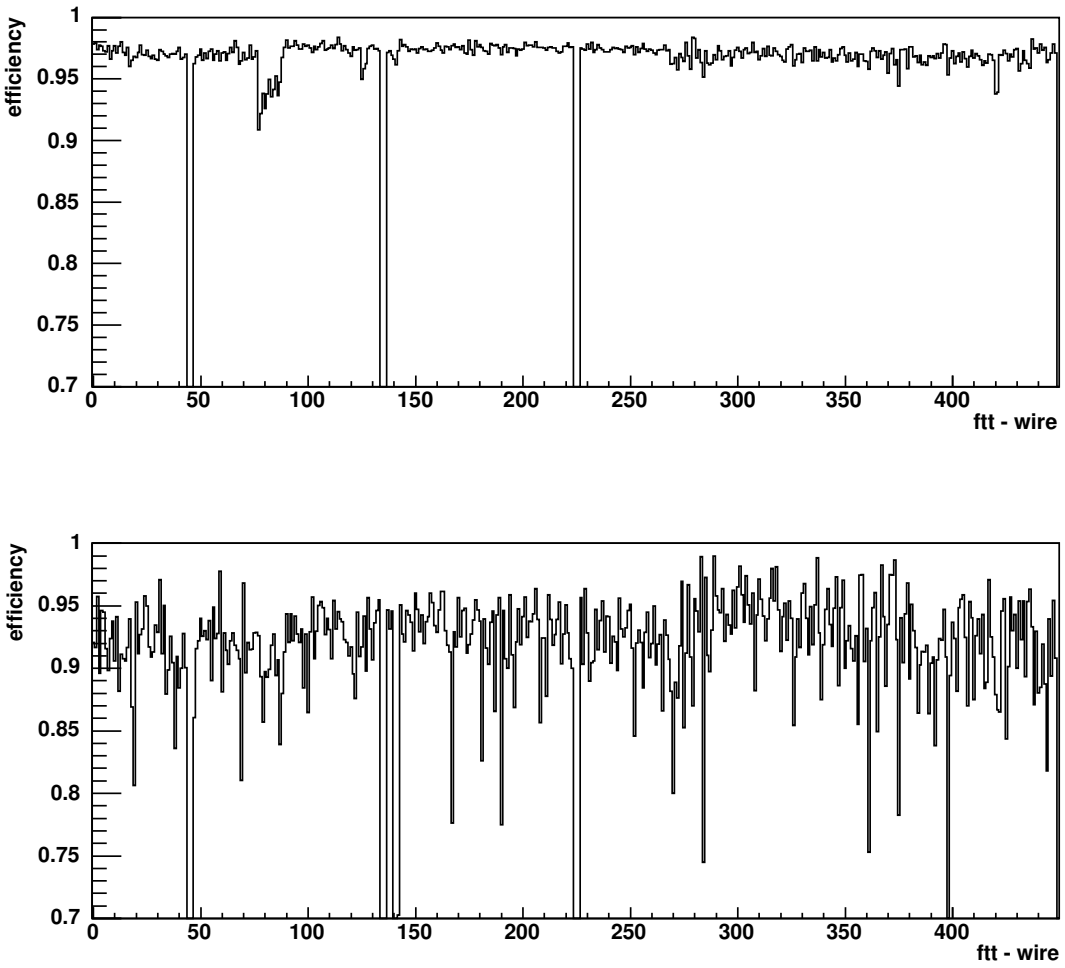

Figure 4.8.: Wire Wise efficiency, obtained by comparison with standard readout (top) and by comparison with reconstructed tracks (bottom). The CJC cell 15 (FTT wires 45-47, 135-137 and 225-227) is identified as inefficient by both methods. In fact the drift time measurement of cell 15 is only shifted, therefore hits in cell 15 don't fulfill the time cut. The middle layer of CJC cell 17 (FTT wires 141-143) is identified only by comparison to tracks.

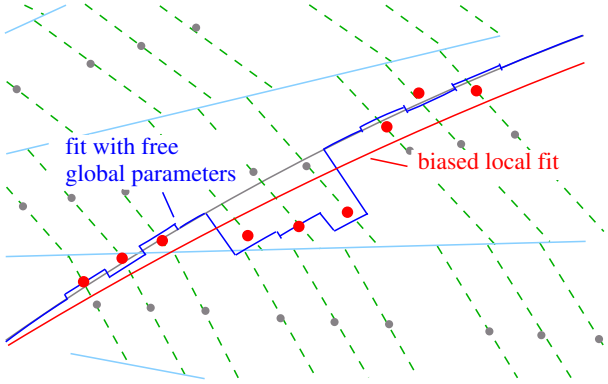

Figure 4.9.: Track fit in the r-φ plane of the CJC with miscalibrated wires. A standard fit and a fit with free global parameters are shown. The global model accounts for the shift of each wire T_0. The visible T_0 shifts would be determined by minimizing the residuals of the shown and many *other* track fits. The difference between the measured hit and the improved model is at the level of the hit resolution.

$$\chi^2 = \sum_{j=1}^{m} \sum_{i=1}^{n_j} \frac{\left(f(x_{i,j}, \vec{L}_j, c_{i,j}, \vec{G}) - y_{i,j}\right)^2}{\sigma_{y,i,j}^2 + \left(f'(x_{i,j})\right)^2 \sigma_{x,i,j}^2}.$$

The full model f depends on the value $x_{i,j}$ of the x coordinate, the parameters $\vec{L}_j$ of the jth local model, and the global parameters $\vec{G}$. It is summed (index j) over m tracks and (index i) the n_i residuals $(f - y_{i,j})^2$ of each track (measurement $y_{i,j}$). Each residual is weighted with the errors $\sigma_{x,i,j}$ and $\sigma_{y,i,j}$ of the x and y coordinates. σ_x^2 is multiplied by the derivative $f'(x)$ with respect to x. The quantity $c_{i,j}$ is the index of the detector 'cell' in which the ith hit of the jth track was detected. The functional form of the global model will typically depend on $c_{i,j}$.

The full model can be decomposed into the sum of the local model f_{local} taken at the coordinate $x_g = f_{x,\text{global}}$ and a contribution from the global model $y_g = f_{y,\text{global}}$

$$f(x) = f_{\text{local}}(x_g, \vec{L}) + y_g, \qquad x_g = f_{x,\text{global}}(x, c_{i,j}, \vec{G}), \qquad y_g = f_{y,\text{global}}(x, c_{i,j}, \vec{G}).$$

The coordinate x_g includes a possible realignment in terms of global parameters. The functional forms of $f_{x,\text{global}}$ and $f_{y,\text{global}}$ are determined by the cell number $c_{i,j}$ and depend on the x coordinate of the measurement and the global parameters.

4.4.3. Linear Least Squares Method and Millepede

Because of the large number of global parameters the minimization of the full χ^2 function can be arbitrarily complicated and time consuming. It is however possible to reduce the complexity of the problem by only considering local and global models with a *linear* dependence on their parameters (linear least squares minimization). This means that non linear models (e.g. a circle as a track model) have to be approximated by a linear Taylor expansion. For local models this is uncritical because adequate initial values for the parameters are known from the uncalibrated reconstruction. In the case of a non linear global model the linear least squares minimization can be repeated iteratively with improving global parameters.

The linear least squares sum has got the general form

$$\chi^2 = \sum_{j=1}^{m} \sum_{i=1}^{n_j} \frac{\left(\vec{L_j} \cdot \vec{d}_{i,j,\text{local}} + \vec{G} \cdot \vec{d}_{\text{i,j,global}} - y_{i,j}\right)^2}{\sigma_{i,j}^2},$$

$$\vec{d}_{i,j,\text{local}}(x_{i,j}, \vec{L}_{j,\text{inital}}, c_{i,j}, \vec{G}_{\text{inital}}) = \begin{pmatrix} \frac{\partial f(x_{i,j}, \vec{L}_{j,\text{inital}}, c_{i,j}, \vec{G}_{\text{inital}})}{\partial L_1} \\ \vdots \\ \frac{\partial f(x_{i,j}, \vec{L}_{j,\text{inital}}, c_{i,j}, \vec{G}_{\text{inital}})}{\partial L_{N_L}} \end{pmatrix},$$

$$\vec{d}_{i,j,\text{global}}(x_{i,j}, \vec{L}_{j,\text{inital}}, c_{i,j}, \vec{G}_{\text{inital}}) = \begin{pmatrix} \frac{\partial f(x_{i,j}, \vec{L}_{j,\text{inital}}, c_{i,j}, \vec{G}_{\text{inital}})}{\partial G_1} \\ \vdots \\ \frac{\partial f(x_{i,j}, \vec{L}_{j,\text{inital}}, c_{i,j}, \vec{G}_{\text{inital}})}{\partial G_{N_G}} \end{pmatrix}.$$

Where $\vec{d}_{i,j,\text{local}}$ and $\vec{d}_{i,j,\text{global}}$ are the derivatives of the local and the global model with respect to their parameters and valid for the ith hit of the jth track. N_L and N_G are the numbers of the parameters of the models. The error $\sigma^2_{x,i,j}$ is neglected for reasons of simplicity so that there is only one error $\sigma^2_{i,j}$ of the measurement $y_{i,j}$. The expressions given above are much simpler for linear models where the dependence on the initial parameters vanishes.

Solution The sum χ^2 is a quadratic function of all free parameters $\vec{a} = (\vec{L}_1, \ldots, \vec{L_m}, \vec{G})$. The solution of the minimization problem is obtained from a set of linear equations (normal equations of least squares). They can be written in matrix form

$$C\vec{a} = \vec{b}, \qquad C = \sum_{j=1}^{m} \sum_{i=1}^{n_j} \frac{1}{\sigma_{i,j}^2} \vec{d}_{i,j} \cdot \vec{d}_{i,j}, \qquad \vec{b} = \sum_{j=1}^{m} \sum_{i=1}^{n_j} \frac{y_{i,j}}{\sigma_{i,j}^2} \vec{d}_{i,j}.$$

Where $\vec{d_{i,j}} = (0, \ldots, \vec{d}_{i,j,\text{local}}, \ldots, 0, \vec{d}_{i,j,\text{global}})$ are the derivatives of the global and local models for the ith hit of the jth track with respect to each of the parameters $\vec{a}$. The parameters of the jth local model only depend on the hits of the corresponding track and therefore most components of $\vec{d_{i,j}}$ are zero. The matrix equation is solved by

$$\vec{a} = C^{-1}\vec{b}$$

4.4.4. Millepede

The software package *millepede* [41] provides an efficient implementation of the method of linear least squares adapted to the needs of a calibration problem. The numerical value of the global and local derivatives of each hit are passed to millepede (routine `equloc`), local fits are completed with `fitloc`. The overall solution is gained by a call to `fitglo`. Millepede uses some special techniques to be able to obtain a fast and precise inversion of the matrix [40].

4.5. z Information

As mentioned in section 2.2.3 the z information of the CJC is determined by measuring the fractional charge on each sense wire end. The ohmic resistance of the sense wire is proportional

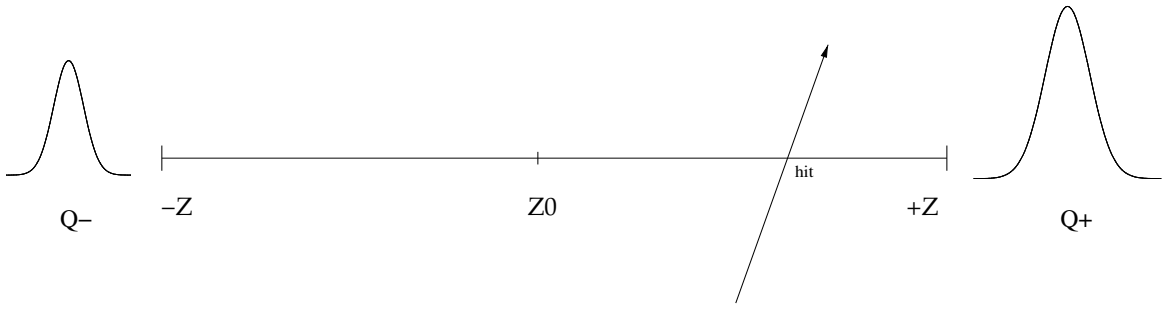

Figure 4.10.: z determination by charge division. The charge measured at the positive (+Z) and negative(-Z) end of the wire depends on the hit position.

to its length. It is of comparable size as the impedance of the rest of the analogue readout chain. The overall impedance and therefore the measured charge of each wire end depends on the z coordinate of the hit. The z position can be calculated from the charge at the positive and negative z wire end Q_+ and Q_- using the expression

$$Z = L_{\text{eff}} \cdot \frac{Q_+ - Q_-}{Q_+ + Q_-} + Z_0.$$

Where L_{eff} is the effective wire length and Z_0 is a global offset of all z values.

4.5.1. Local Model

As mentioned above the form of the track is called local model in the terminology used by millepede. The track is described by a straight line in s-z space

$$Z(s) = Z_0 + s \cdot m_Z,$$

where s is the arclength measured along the circular track. The magnetic field has no influence in the s-z plane, because it is parallel to the z direction. The derivatives of the local model needed for the linear least squares sum are

$$\frac{\partial Z}{\partial Z_0} = 1$$

$$\frac{\partial Z}{\partial m_Z} = s$$

4.5.2. Global Model

As the uncertainty of the s coordinate is negligible compared to the error of z the effect of the global model is reduced to an additive term ΔZ in the total model $Z = Z(s) + \Delta Z$. It formalises the lack of knowledge about the precise value of the effective wire length L_{eff} and the offset Z_0.

$$\Delta Z = \Delta L_{\text{eff}} \cdot \frac{Q_+ - Q_-}{Q_+ + Q_-} + \Delta Z_0$$

Where ΔL_{eff} are ΔZ_0 the corrections to the parameters used for the initial z calculation. The derivatives needed for millepede are

$$\frac{\partial \Delta Z}{\partial \Delta L_{\text{eff}}} = \frac{Q_+ - Q_-}{Q_+ + Q_+}$$

$$\frac{\partial \Delta Z}{\partial \Delta Z_0} = 1$$

The simple form of all derivatives arises from the linearity of the models and their uniformity for all wires.

4.5.3. z Resolution

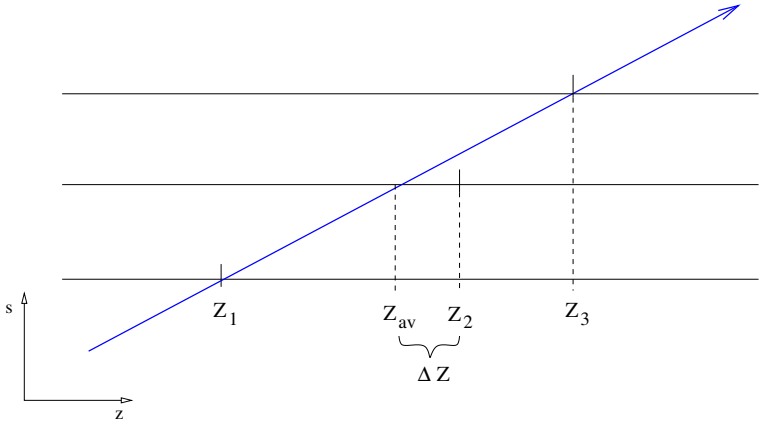

Figure 4.11.: s-z view of a track in a FTT cell. The difference between the averaged z value of the outer wires and the z value on the middle wire is a measure for the z resolution.

For the correct application of the linear least squares method the weight of each residual has to be known beforehand. The resolution of the charge division method is measured by considering hit tripletts in FTT cells, compare figure 4.11.

The averaged coordinate $z_{av} = \frac{z_1+z_3}{2}$ is interpreted as an estimator for the real track position at the middle wire. Its rms error σ_{av} is $\sigma_{av} = \sigma_z/\sqrt{2}$ (error of mean), where σ_z is the unknown z resolution. The variance $\sigma_{\Delta z}$ of the difference between the z_{av} and Z_2 is obtained by quadratically adding the errors of z_{av} and Z_2

$$\sigma_{\Delta z} = \sqrt{3/2} \cdot \sigma_z.$$

$\sigma_{\Delta z}$ is obtained by a Gaussian fit, compare figure 4.12. In order to account the z dependence of the resolution the fit procedure is repeated for three bins in $|z|$. During the development of the calibration software performed in this thesis the resolution fits were repeated with an adjusted average effective wire length obtained in first calibration attempts.

4.5.4. Track Selection

The z calibration is performed by feeding tracks of muons of the cosmic radiation (cosmics) into millepede. Cosmics provide a flat distribution in z which is necessary for a precise calibration. Tracks of particles produced in ep interaction on the other hand mainly originate from the center of the chamber. They don't provide hits at the outer z regions of the inner wires, which are

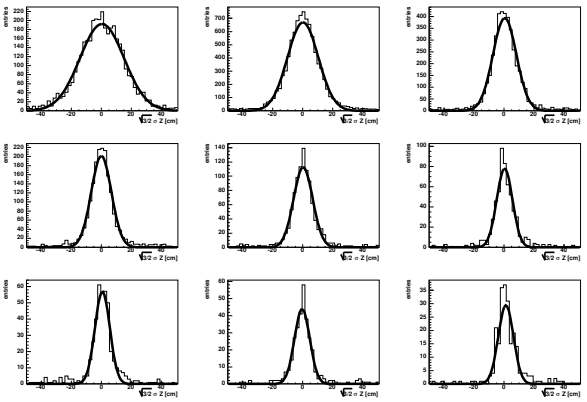

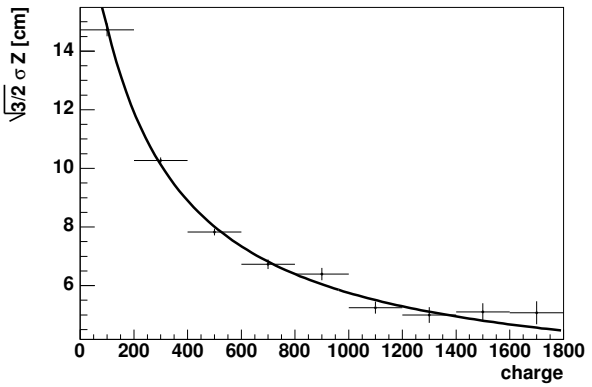

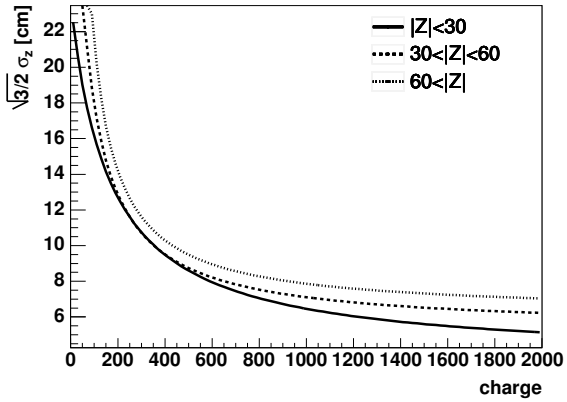

Figure 4.12.: *Top Left*:Z resolution needed for the calibration as obtained by considering hit tripletts. The difference between the averaged z coordinate and the z position on the middle wire is fitted in different bins of charge. *Top Right*: The variance of the Gaussian fits is shown as function of charge Q (top right). The charge dependence is nicely described by a fit of the form $\sqrt{3/2}\sigma_z = a/(Q-b)+c$. The z resolution determination is repeated for three bins in $|z|$(bottom left).

Table 4.2.: Track cuts used for the z calibration procedure

cut	comment
$(0.003 \cdot 1.15)/\kappa > 0.5\frac{\text{GeV}}{c}$	A minimal transverse momentum reduces multiple scattering and is necessary for the track to pass trough both chambers.
$Z_0 < 95\text{cm}$	cut on z at d_{ca}
rStop−rStart $> 30\,\text{cm}$	A minimal track length is an indication for good tracks.
$30° < \Theta < 150°$	The polar angle is restricted to the FTT acceptance.
$300 < T_0 < 600$	A soft timing cut is applied, because the r-φ information is not critical.
$\chi^2 < 1.5$	χ^2 over number of degrees of freedom has to be compatible with expectation.
dΘ<0.06	Cut on the parameter errors obtained in the fit, see text.
d$Z_0 < 3.7\,\text{cm}$	
dφ<0.02	

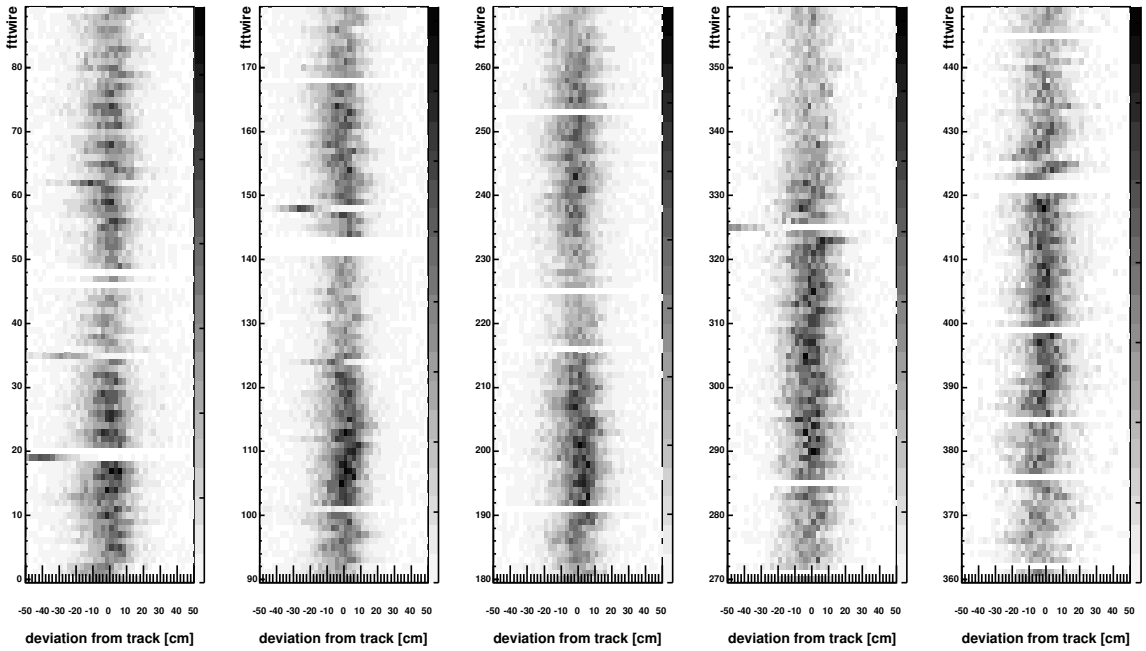

Figure 4.13.: The uncalibrated deviations from the track expectation in the s-z plane are shown for each FTT wire. The histograms show (left to right): the 1st, 2nd and 3rd layer of FTT wires in the CJC1 and the first and second half of the 4th layer in CJC2. The residuals are obtained with an effective wire length of 220 cm. The white bars in the histogram originate from wires without or with unusable z measurement. Most of them have a broken preamplifier on one wire end.

necessary to determine the effective wire length. A number of cuts are applied to the cosmic track sample, they are summarized in table 4.2. The cuts on the parameters errors ($\mathrm{d}\Theta$, $\mathrm{d}Z_0$, $\mathrm{d}\varphi$) obtained by the fit during the offline reconstruction are selected by looking at the distribution of these errors. The limits are chosen such that events in the tail of each distribution are discarded.

The hits of an accepted track are identified by requiring a drift distance in agreement with the track position (r-φ plane) within a range of 0.5 mm. Also, the total charge of each hit is restricted to lie in the range $200 < Q < 4000$. Outliers in the z plane are automatically identified and discarded by the millepede algorithm. The resolution of each z measurement σ_z is determined depending on the charge and z position and is taken from the resolution fits (subsection 4.5.3).

The tracks obtained by the full offline reconstruction contain z information from all CJC wires and eventually other tracking detectors. In order not to waste this precise knowledge by refitting the tracks just to the FTT z information additional 'artificial hits' are added to each local fit. An additional hit is added for each CJC wire crossed by the track. The parameter error $\mathrm{d}Z_0$ is assumed as uncertainty σ_z of each hit recalculated from the track parameters.

4.5.5. Results

Figure 4.13 shows the deviations of the FTT z coordinates from the tracks of the offline reconstruction. The z values are obtained using an average effective wire length of 220 cm. After

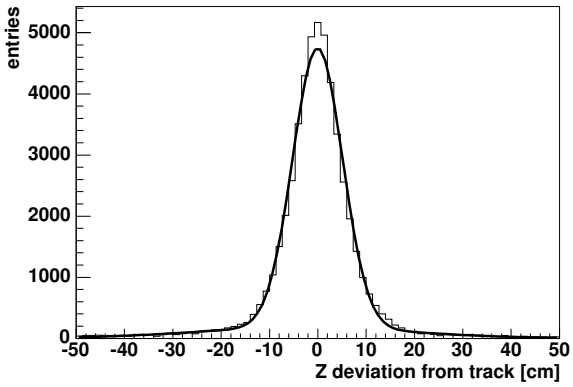

Figure 4.14.: Difference between FTT z measurements and the track fit using the corrections obtained by millepede. The double Gaussian fit results in a core width of 5.2 cm (mean-4×10^{-2} cm). A charge of more than 400 units is required in order to be able to compare the measurement to figure 4.12.

applying a correction for the global parameters the deviations are reduced and nicely lined up (figure 4.16). In figure 4.14 a Gaussian fit to the z residuals is shown for hits with a charge of more than 400 units. The width of the distribution is found to be 5.2cm.

4.6. Drift Time Calibration

The drift times stored in the monitor data of the FTT have been measured by the Qt algorithm and encoded and regained from shift registers. They are displaced by a value determined by details of the implementation of the firmware. Also, the signal needs some hidden time to propagate through the analogue electronics which may slightly differ from wire to wire. Altogether the measured drift time T is composed of the real drift time T_{D} and a shift T_0^i which has to be determined for each wire individually

$$T = T_{\mathrm{D}} + T_0^i.$$

4.6.1. Local Model

In order to simplify the local model the measured quantity which is feed to millepede is not the absolute value of the each measured drift time but its deviation ΔT from the offline fitted track. Assuming small alignment corrections a local model has got the form of a difference between two similar circles. It can be adequately described by a parabola in certain coordinates (compare figure 4.18)

$$\Delta T = \left(\Delta\kappa \cdot 2 \cdot \left(\frac{\sin(s \cdot \kappa/2)}{\kappa} \right)^2 + \Delta\varphi \cdot (1 - \kappa \cdot d_{ca}) \cdot \frac{\sin(s \cdot \kappa)}{\kappa} + \Delta d_{ca} \cdot \cos(s \cdot \kappa) \right) \frac{1}{\cos\beta}.$$

Where κ, φ and d_{ca} are the track parameters, s is the track length where the hit is measured, β is the angle between the drift direction and the track and $\Delta\kappa$, $\Delta\varphi$ and Δd_{ca} are the corrections to the offline track fit.

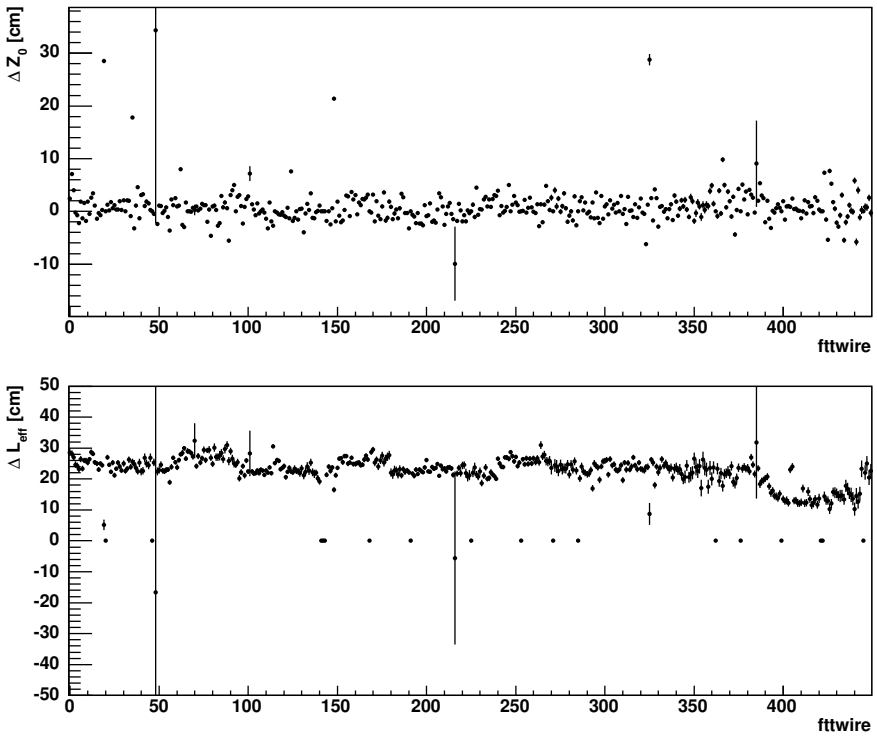

Figure 4.15.: Global parameters obtained by millepede for each FTT wire: ΔZ_0(top) and ΔL_{eff}(bottom).

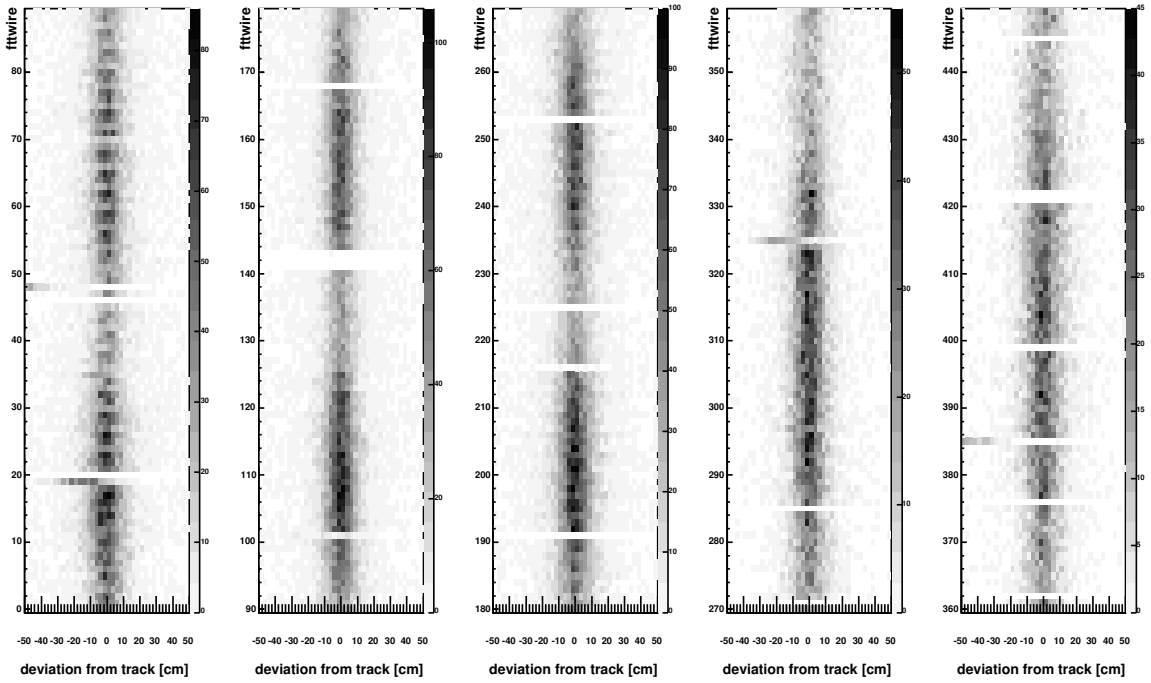

Figure 4.16.: Deviations in z from the offline track fit after applying millepede corrections are shown for each FTT wire. Compared to figure 4.13 a improved and unbiased z values are obtained.

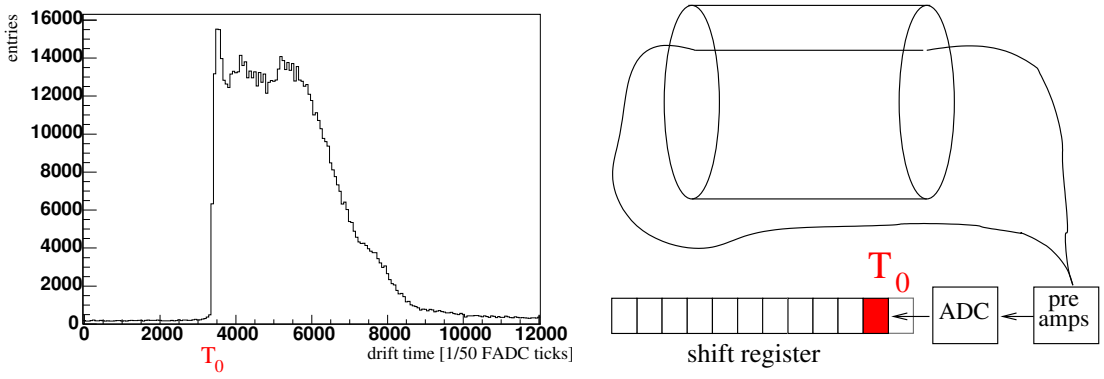

Figure 4.17.: Left: Uncalibrated drift time spectrum of all wires. The T_0 which is approximately equal for all wires can be seen as rising edge of the spectrum. The soft drop is caused by the dependence of the maximal drift time on the CJC layer. Right: The analog signal propagates through some electronics before arriving at the digitizer, where signal time is measured.

4.6.2. Global Model

The dependence of each drift time on a variation of the T_0 offset of the ith wire ΔT_0^i and on the variation of the drift velocity is

$$\frac{\partial T}{\partial \Delta T_0^i} = 1$$

$$\frac{\partial T}{\partial \Delta v} = T_{\mathrm{D}}.$$

The effect of the relative alignment of both chambers and the effect of a Lorentz angle variation are a bit more sophisticated. They are calculated from the point of intersection of the track and the drift route to the sense wire. The drift time is computed from the point of intersection and is derived with respect to

- the variation of the wire position in x and y direction,
- the angle $\Delta\varphi$ of a rotation of the chamber around the z axis
- the drift direction variation ΔL_A(Lorentz angle)

There is an implementation of these computations which is available for the calibration of the standard readout (h1rec routine `cjxdrd`). It is used to obtain the numerical values of the derivatives listed above as a function of the track parameters and the wire number.

Also the drift time resolution needed for millepede is adapted from the standard readout calibration routines. It is read from the FORTRAN common block `CJDCAL` depending on the wire number and the drift distance. The absolute values for the standard readout are slightly lower than the resolution of the FTT readout. The reason for this is the fixed bin width of the FTT readout. Nevertheless do the effects, that degrade the resolution near the chamber walls and for long drift distances, effect both readouts in the same way. The relative weight of the data points is therefore described sufficiently precise.

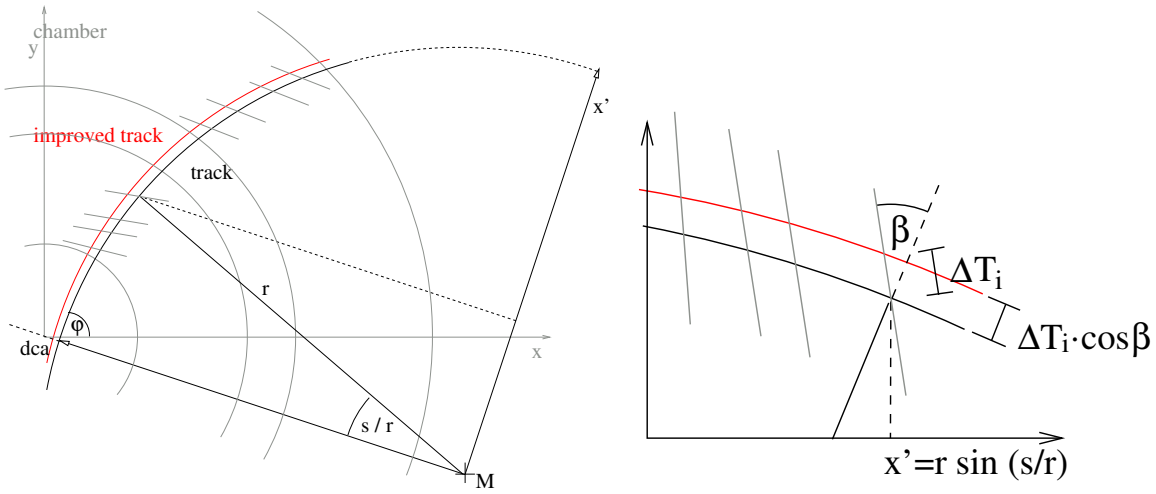

Figure 4.18.: The residuals ΔT are measured in a coordinate system defined by the track: $x' = r \cdot \sin(s/r)$ and $\Delta T' = \Delta T \cdot \cos\beta$, where β is the angle between the drift vector and the radial direction (r) of the track. M is the center of the circle describing the track and $r = 1/\kappa$ is its radius.

Table 4.3.: Track cuts used for the drift time calibration procedure

cut	comment
$(0.003 \cdot 1.15)/\kappa > 0.6\,\frac{\text{GeV}}{c}$	At low transverse momenta multiple scattering smears the track trajectories.
$Z_0 < 50\,\text{cm}$	Discards tails of the Z_0 distribution
rStop−rStart $> 40\,\text{cm}$	Only tracks which can be fitted with a single trajectory reaching through both chambers are taken into account.
$30° < \Theta < 150°$	The polar angle range is restricted to the FTT acceptance.
$445 < T_0 < 465$	The event T_0 (subsection 2.2.3) has to compatible with tracks originating from an ep interaction.
$\chi^2 < 1.5$	χ^2 over number of degrees of freedom has to be compatible with expectation.
dφ<0.01	Good quality of the track fit in the r - φplane.
$d_{ca} < 12\,\text{cm}$	The cell geometry is optimized for tracks originating from the interaction region.

4.6.3. Track Selection

The drift time calibration is performed using high quality tracks recorded in ep collisions. A certain transverse momentum is necessary, because multiple scattering leads to a smearing especially of low p_t tracks (Compare also Appendix A). The value of $0.6\,\frac{\mathrm{GeV}}{c}$ is choosen as a compromise between track quality and the number of accepted tracks for the calibration. The T_0 discards tracks caused by cosmic muons, as they need special treatment. The other cuts (Z_0, χ^2, dφ, d_{ca}) are choosen in order to reject outliers in the respective distributions and to assure a good track quality.

4.6.4. Results

Figure 4.19 shows the deviation of the drift times from the tracks of the offline reconstruction. It can be seen that the drift times of the 15th trigger group are shifted with respect to the T_0 of the other groups. The overall variance of the uncalibrated residual distribution is roughly $450\,\mu$m.

As mentioned in subsection 2.2.3 the chamber configuration of the CJCs leads to an spatial ambiguity of the measured hits. Some of the global alignment parameters effect the drift time measurement depending on the side of the sense wire plane on which the hit was measured. Figure 4.20 shows the effect of the corrections of the different global parameters for hits on the negative[4] side of the sense wire plane. The improvement obtained from each correction can be clearly seen. In figure 4.21 the final calibrated residuals are shown for the different FTT layers.

A Gaussian fit to the distribution 4.22 of the calibrated residuals yields a variance of $340\,\mu$m. For comparison the FTT calibration procedure is applied to hits (on FTT wires) measured by the standard readout. In this case the final resolution fit results in variance of $230\,\mu$m, which has to be compared with the design resolution of $170\,\mu$m. Possible worsening factors could be too loose criteria on track quality or a limit on the calibration precision arising from the missing CJC wires in the FTT readout.

On the other hand the r-φ resolution of the FTT readout is determined by the granularity $d = 625\,\mu$m of the drift time discretisation in the shift registers. Assuming a uniform distribution in the 80MHz bins of the registers a resolution somewhere between the 68% containment error ($0.68 \cdot 625\,\mu$m) and root mean square error ($1/\sqrt{12}[\approx 0.29] \cdot 625\,\mu$m) can be expected. The measured value of $340\,\mu$m is in between these two numbers.

[4]The sense wire sides are labeled according to the fact whether the hits lie in the direction of the drift vector or the opposite (negative) direction.

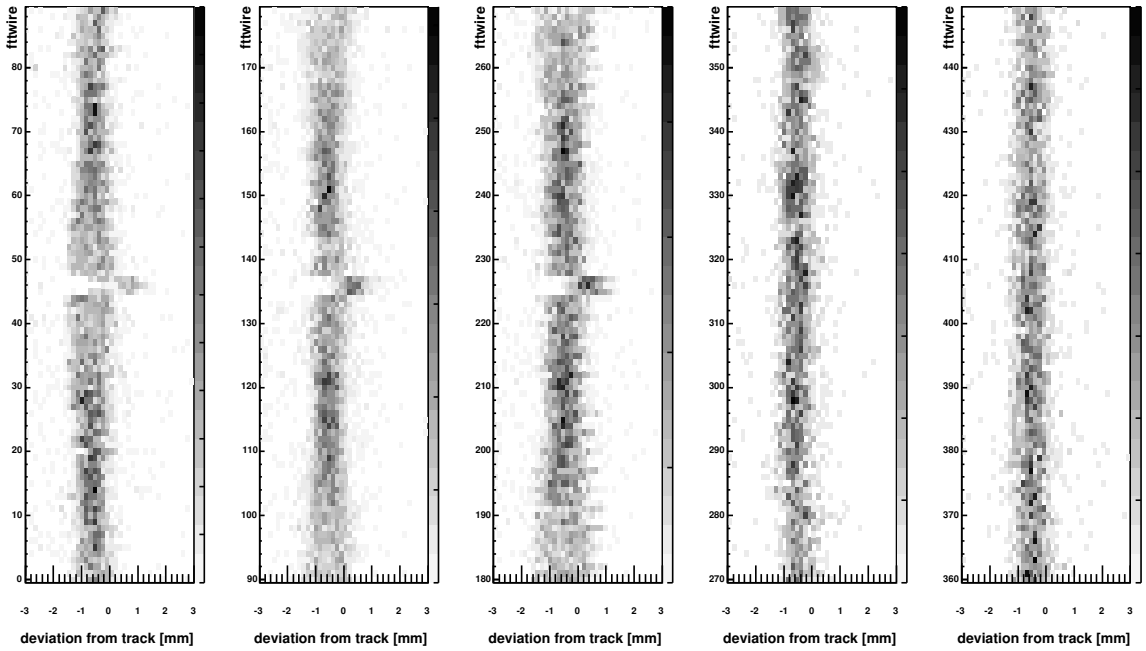

Figure 4.19.: The uncalibrated deviations of the drift time from the track expectation in the r-φ plane are shown for all FTT wires. The wires showing a differing T_0 offset are situated in cell 15 of CJC-1.

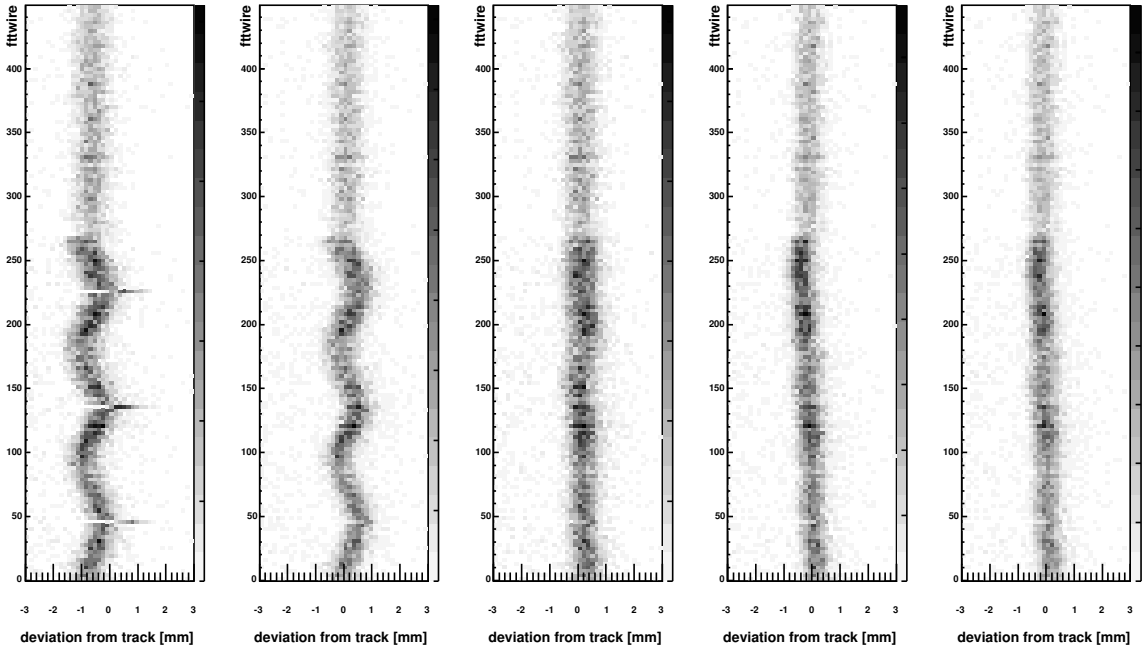

Figure 4.20.: The effect of the different calibration corrections on hits at the negative side of the sense wire plane is shown for all FTT wires. The leftmost plot shows the uncorrected residuals. From left to right the T_0 offset corrections, the alignment (x and y shift, φ rotation) corrections, the drift velocity corrections and finally the Lorentz angle corrections are applied.

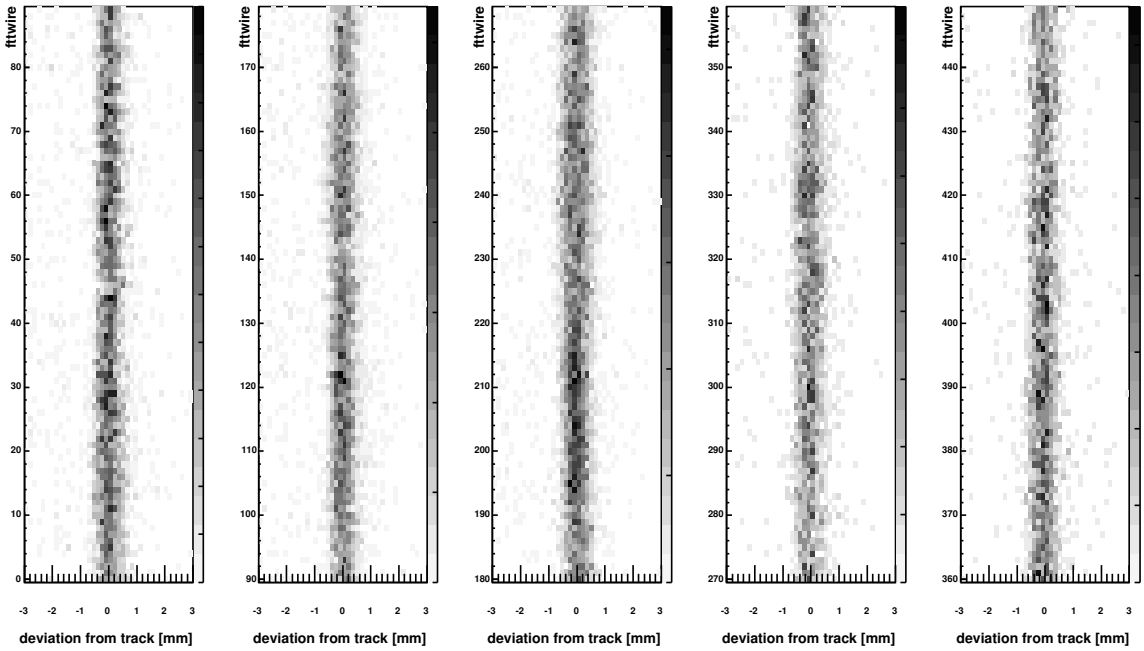

Figure 4.21.: The calibrated drift time residuals are shown for each FTT wire. The resolution is improved and all hits lie nicely on top of the track expectation.

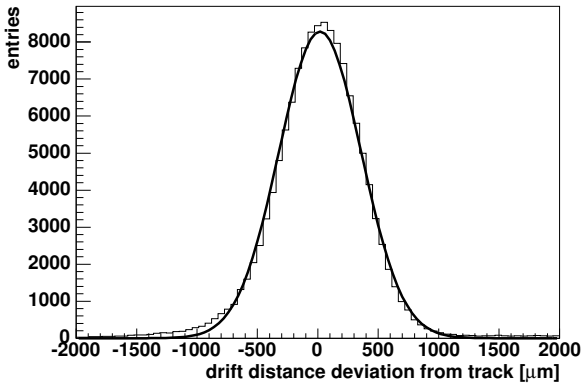

Figure 4.22.: The difference between the measured drift time and the track is shown for all hits. The Gaussian fit has got a variance of 340 μm (mean is 18 μm)

5. Commissioning

5.1. VME performance

As mentioned in section 3.4 the readout of the monitor data is controlled by the crate master PowerPC boards. The data is read from the electronic boards via the VME backplane bus of the crate and passed to the readout chain. During the 2004 data taking period the FTT system had to struggle with some readout performance problems. It turned out that the readout throughput was limited by the VME transfer.

The performance of different transfer modes which can be used to obtain the data over the VME bus was studied in order to find ways to improve the readout capacity. Also, the speed of a new optimized VME interface which is providing the bus access on the custom board (MPB, FEM) side was measured.

5.1.1. VME versus compact PCI

VME Bus is widely used as backplane bus in electronic crates. During the design of the FTT system the VME bus was favoured over a compact PCI (CPCI) solution. Reasons were the better availability of VME CPU boards and the good experiences collected with VME systems in H1 . In contrast CPCI has never been used in the H1 trigger/DAQ. The data transfer rate according to specification is comparable for both systems (up to 40-80 MB/s for VME and 132 MB/s for CPCI). The performance of the VME bus depends on the bit depth of the data words, which is restricted to 16 bit by the backplane connectors in case of FEM and MPB boards. The L3 crate uses 32 bit words in VME transfers [31].

5.1.2. Measurement Procedure

Routines were written which transfer a number of words using the transfer modes summarized in table 5.1. The time needed for a bus cycle is measured during a series of transfers. This is done by directly observing the connections in the backplane of the crate with the help of a logic analyzer (compare figure 5.1). In case of DMA and DMA-Block transfers the time needed to initialize the transfer is also measured.

5.1.3. Results

It can be seen that read cycles are generally slower than write cycles. This is caused by the additional time needed to provide the data to be transferred. The bandwidth reached using the new VME interface with standard (non-DMA) transfer is less than 2 MB/s. The transfer rate of the VME Interface is restricted by two factors: The time the VME Interface on the electronic card needs to get the data over local bus and the time the CPU board needs to adopt the data. This means basically that further improvement of the interface can not be expected.

By using DMA transfer the data adoption time can be improved. The bandwidth is increased roughly by a factor of two with the drawback of additional initialization time. In addition, the CPU is available for other tasks during the DMA transfer. This may be an advantage although not crucial during the readout.

It should be mentioned, that DMA transfer is limited to blocks of adjacent VME addresses. This means in order to read addresses that are not "blocked" together, the DMA transfer has to be initialized several times. To partly overcome this problem it is possible to use the linked list mode of the UNIVERSE II [42] VME bridge. A list of VME address blocks is passed to the chip, which then is able to reduce the reinitialization time during the transfers down to $2.3\,\mu$s. The linked list mode is not supported by the board support package[1] (BSP), which means that routines using it will only work with certain CPU boards, containing the UNIVERSE II chip.

The last option taken into consideration is block mode. Block mode is a modification of the VME transfer protocol, such that when reading blocks of adjacent addresses (as anyway necessary for DMA transfer) only the starting address and and size of the block have to be transmitted to the source. The block transfer mode has to be supported by the receiving and the sending VME device (unlike the different DMA transfers which are internal modes of the CPU boards).

5.1.4. Which Mode to Use

The optimal mode depends on the size of the blocks of adjacent VME addresses to read or write. If it is necessary to read single separated addresses, the simple CPU based transfer is already fastest.

Linked list and normal DMA Mode differ in the reinitialization time needed between address blocks. Therefore linked list mode is reasonable for small address blocks, while the advantage is negligible for big blocks.

With the numbers obtained it can be easily computed, that for blocks of *8* Bytes or more, the improvement of linked list mode is bigger than 25%. On the other hand when transferring blocks of more than *112* Bytes the time saved by using linked list mode instead of normal DMA transfer (which is supported by the BSP) drops less then 10%.

$$\begin{aligned} 2.3 + 0.6 \cdot N &< 75\% \cdot (1.2 \cdot N) \\ N &> \frac{2.3}{0.75 \cdot 1.2 - 0.6} \approx 7.6 \end{aligned}$$

$$\begin{aligned} 2.3 + 0.6 \cdot N &< 90\% \cdot (10 + 0.6 \cdot N) \\ (0.6 - 5.4) \cdot N &< 9 - 2.3 \\ N &< \approx 111.6 \end{aligned}$$

5.2. Commissioning of the Merger

As described in appendix B.2, the merger has the task to multiplex the input data of six FEMs to single data stream passed to the linker. The merger has a L1 and a L2 mode, because of the different protocols used for the segment transmission. As there is no actual data processing on the merger, no monitoring data is read out from the merger. On the other hand are the tedious timing requirements especially of the L1 mode a quite critical point of the system. This is one reason why the merger was tested extensively before installing it in the experimental hall. In the context of this work test pattern were acquired and used with merger test setup in the trigger laboratory.

[1] The BSP is a set of routines building up a defined interface to certain hardware functionality of CPU boards.

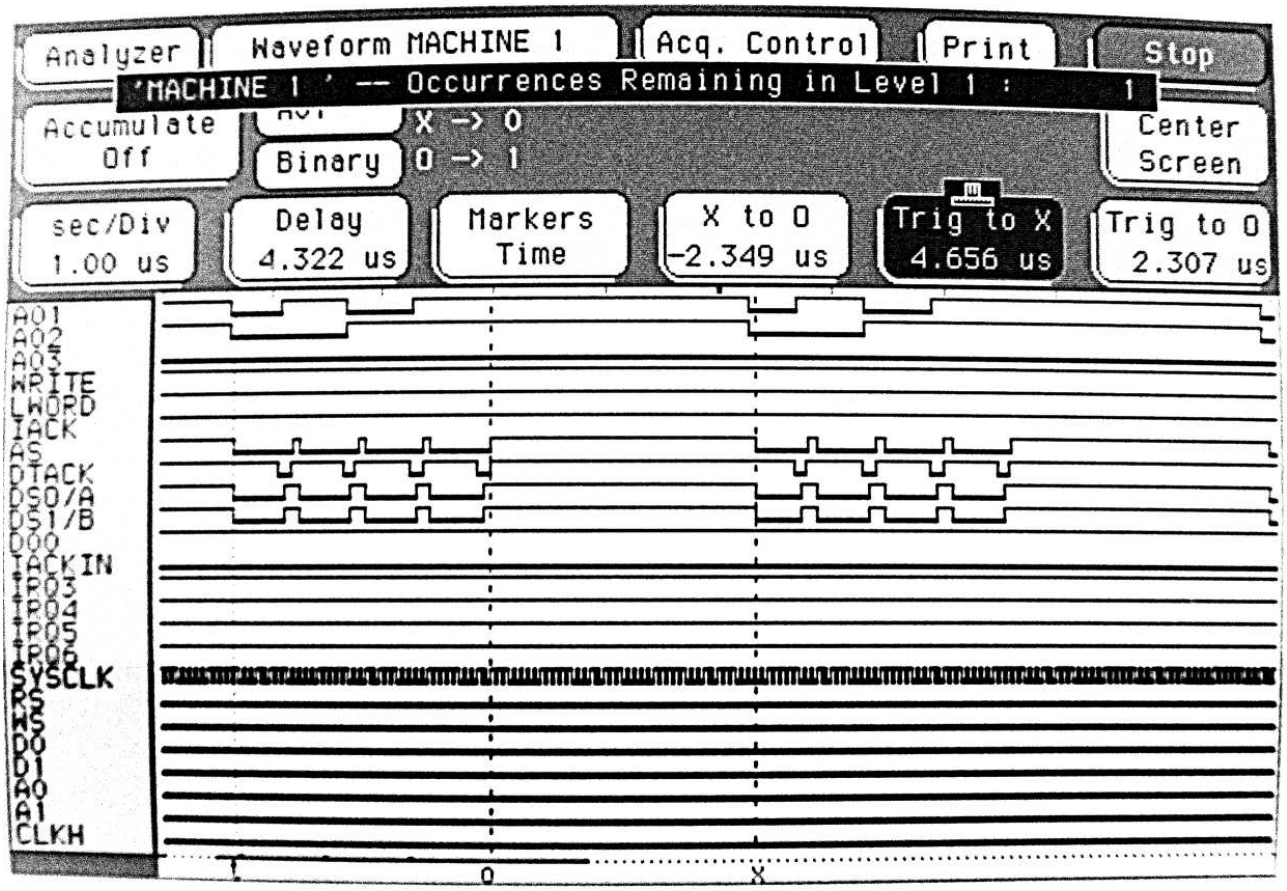

Figure 5.1.: A VME transfer is observed with a logic analyser. The activity of the electrical connections shows the periodicity of the read cycles. The time needed to initiate the next transfer is measured by the markers (0 and x).

Table 5.1.: Summary of DMA-cycle times for different transfer modi. Standard DMA transfers cannot be started more often than every 30..50 μs. But because the CPU is available during the transfer, the preparation the next address block can be done in parallel. The minimal delay in this case is around 10 μs

	Init Time [μs]	Read [μs]	Write [μs]	read bandwidth [MB/s]
Old Interface	-	1.6	1.0	1.2
New Interface	-	1.2	0.7	1.7
Standard DMA	10-50	0.6	0.27	**3.3**
Linked List DMA Mode	2.3	0.6	0.27	**3.3**
Block Mode DMA	LL Standard	0.31		6.5

5.2.1. Test Setup

In order to test the data flow through the merger board the input data streams have to be generated and the output has to be recorded somewhere. An MPB equipped with 4 i/o PB cards which is called 'tester' is used for this purpose. As four i/o PBs can only provide four output ports the i/i cards of the merger have to be equipped with special firmware which doubles the input from the tester connection. Each output port of the tester is connected to the corresponding input port on the merger. The two output ports of the merger are connected to the corresponding input ports on the tester.

The tester is equipped with a FIFO of 128 words length for each in and output port. The tester is controlled with the help of the FTT graphical user interface (GUI). The output queues can be loaded by loading a test pattern into the gui and transfering it to the tester (using the `<setup>` button). `<setup>` also clears the input queues of the tester, and thus enables it to receive new data.

5.2.2. Test Pattern

The L2 test pattern comprises an introductory control word consisting of 0xF8 and a HERA clock value. The finishing control word is composed of 0xFF followed by the number of sent segments. Between the control words there are 'L2 segments' which are choosen such, that the PB on which they are received is encoded in their (otherwise abritrary) value.

The complete L1 merging protocol is depicted in figure B.3. As parts of the L1 segments are mixed during the 'multiplexing' each Byte of an L1 segment contains the information about its position in the input data stream, compare table 5.2

Table 5.2.: Merger test pattern

L2 Test Pattern	
Gui Input File	**description**
∗ first FiFO	Comments wih ∗
f80000123456	Control word
081111111111	L2 Segments
081111111112	.
.	.
.	.
.	
081111111118	
081111111119	
08111111111A	
FF000000000A	No more seg. word
! NEXT PB	Instruction for
∗ second FIFO	Gui: next FIFO
f80100123456	
302222222222	
382222222223	
402222222224	
482222222225	
502222222226	
FF0100000005	
! NEXT PB	
f80200123456	
583333333331	
583333333332	
.	
.	
.	
58333333333A	
FF020000000A	
! NEXT PB	
f80300123456	
804444444444	
884444444445	
904444444446	
984444444447	
a04444444448	
FF0300000005	

L1 Test Pattern	
Gui Input File	**description**
F80000123456	Begin Trigger Data
0A0102030405	κ lower bytes
0C060708090A	κ higher bytes
090000000000	empty word
090000000000	empty word
121111111111	z segment group 0
141212121212	z segment group 1
181414141414	z segment group 2
090000000000	empty word
090000000000	empty word
! NEXT PB	Gui: Next Fifo
F80100123456	wie oben
0A28292A2B2C	
0C2D2E2F3839	
090000000000	
090000000000	
122121212121	
142222222222	
182424242424	
090000000000	
090000000000	
! NEXT PB	
F80200123456	
0A48494A4B4C	
0C4D4E4F5859	
090000000000	
090000000000	
124141414141	
144242424242	
184444444444	
090000000000	
090000000000	
! NEXT PB	
F80300123456	
0A88898A8B8C	
0C8D8E8F9899	
090000000000	
090000000000	
128181818181	
148282828282	
188484848484	
090000000000	
090000000000	

6. Summary

H1 collected a big amount of inclusive data in the whole accessible kinematical range during the HERA I running periods. The HERA II upgrade aims mainly at the exploration of the remaining areas of low cross section processes. Among those there are ep events at highest four momentum transfers and exclusive final states like heavy quark production. In order to cope with the increased background and ep interaction rates the selectivity of the trigger had to be improved. The identification of interesting processes in the bulk of low Q^2 events requires precise track information already on trigger level. The FTT uses the hit information of the CJC that is not avalaible before the end of the maximal drift time, equal to the half of the L1 latency of 2.3μs. The FTT provides track based trigger information to the first three trigger levels of H1. A two dimensional track reconstruction is the basis for the L1 decision. During the L2 latency of 22μs a precise three dimensional fit of up to 48 tracks is performed. For the first time in H1 the FTT is going to implement the third trigger level. The L2 tracks which are approaching offline precision are used to compute invariant masses of particle decays on the third level.

The high precision of the reconstruction requires a precise calibration of the input data. In the context of this work calibration procedures were implemented for the drift time and for the z information. The drift time calibration takes into account the wire wise T_0 offset, the relative alignment of CJC1 and CJC2 and variations of the drift velocity and Lorentz angle. A calibration of the z information determines the effective wire lengths and z shifts needed for the z extraction by charge division.

Also, tools were developed for the analysis of the FTT monitoring data in an object oriented fashion. A graphical display for the FTT raw data and the Qt algorithm is integrated into this framework. The tools were used to measure the single hit efficiency with various methods: the hits found by the FTT front end are compared to hits of the standard readout. Also, the ratio of hit tripletts and dobletts in a trigger cell is studied. Finally, the FTT hits are compared to offline reconstructed tracks fulfilling certain quality cuts.

During the commissioning of the first level of the FTT system studies were made about the performance of different VME transfer modes. The firmware of the merger MPB board was tested. Service routines for the Multi I/O card providing the L3 crate with signals from the central trigger logic were written.

A. Tracker Resolution

The angular and (transverse) momentum resolution of a magnet spectrometer is mainly determined by two effects: the intrinsic *spatial resolution,* and the amount of direction smearing caused by *multiple scattering*[1] (MS) of the traversing particle. An analytic estimation of both effects is possible:

- The uncertainties of space point measurements can be propagated onto the fitted particle direction and momentum.
- The effects of MS are calculated according to [43].

The formulas obtained by Gluckstern are summarized and converted into the form used for the plots A.2 on page 57.

A.1. Errors in p_t and Direction

The projection of the particle trajectories (length L) onto a plane perpendicular to the magnetic bending field is described by a circle with the radius $R[m] = \frac{p_t[\mathrm{GeV}]}{0.3} B[T]$ (magnetic field strength B). For high transverse momenta ($p_t \sim R \gg L$), where the measurement is limited by spatial resolution, a parabolic approximation $y = a + bx + \frac{1}{2}cx^2$ (compare figure A.1) to the circular track is valid. The track fit can be ascribed to a *linear* minimisation problem in this approximation. This allows for the estimation of the covariance matrix V of the parameters a, b, c. The covariances σ_{ij} are only depending on the detector resolution in transverse plane $\sigma_{r\varphi}$, the track length L and the number of equidistantly measured space points N. For $N \gtrsim 10$ the following approximations hold [43]:

$$\sigma_c^2 = \frac{\sigma_{r\varphi}^2}{L^4} \cdot \frac{720}{N+5} \qquad \sigma_b^2 = \frac{\sigma_{r\varphi}^2}{L^2} \cdot \frac{192}{N+4.9} \qquad \sigma_{bc} = -\frac{1}{2} \cdot \frac{\sigma_{r\varphi}^2}{L^3} \cdot \frac{720}{N+5}.$$

Note that the paramters b and c are correlated ($\sigma_{bc} \neq 0$). Using $p_t = 0.3 \cdot R \cdot B$ and $1/R = \kappa \approx c$ one obtains by Gaussian error propagation:

$$\left(\frac{\sigma_{p_t}}{p_t}\right)_{\mathrm{res}} = p_t \cdot \frac{\sigma_{r\varphi}}{0.3 \cdot BL^2} \sqrt{\frac{720}{N}}$$

[1] Elastic scattering in the coulomb field of nuclei.

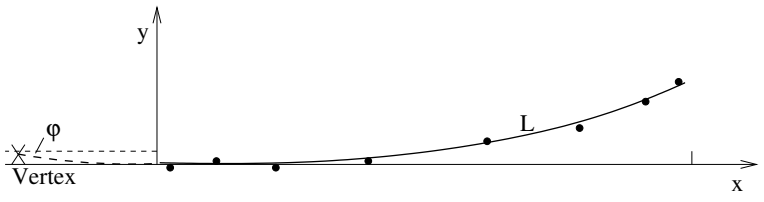

Figure A.1.: coordinate system for the track fit

and accordingly $\varphi \approx \tan\varphi = \left.\frac{\partial y}{\partial x}\right|_v = c \cdot x_{\text{vertex}} + \theta$ leads to:

$$\sigma_\varphi^2 = \frac{\sigma_{r\varphi}^2}{L^2} \cdot \left\{ \frac{720}{N+5} \left(\frac{x_{\text{vertex}}}{L}\right)^2 + \frac{192}{N+5} - \frac{1}{2} \cdot \frac{720}{N+5} \frac{x_{\text{vertex}}}{L} \right\}.$$

The φ resolution depends on the distance of the tracking device to the interaction point (vertex). It can be simplified further by assuming a certain vertex position (e.g. $x_{\text{vertex}} \approx -0.25\,L$ for H1):

$$(\sigma_\varphi)_{\text{res}} \approx \frac{\sigma_{r\varphi}}{L} \cdot \sqrt{\frac{147}{N+5}}.$$

A.2. Multiple Scattering Errors

According to Molière theory the r.m.s of the the projected scattering angle can be calculated by

$$\sigma_{\text{scat}}^2 = \left(\frac{13.6\text{MeV}/c_{light}}{\beta\, p} \right) \cdot \frac{d}{X_0}$$

for given particle momentum p, thickness of traversed material d, its radiation length X_0 and assuming $\beta = v/c_{light} \approx 1$, where v is the velocity of the particle and c_{light} is the speed of light. The variation of displacement and its correlation with the angle can be described by similar expressions. Combining all those with the outcome of the linear least squares ansatz on obtains the following results [43], holding again for $N \gtrsim 10$:

$$\sigma_c^2 = \frac{1.43}{L^2} \cdot \sigma_{\text{scat}}^2, \qquad \sigma_b^2 = 0.23 \cdot \sigma_{\text{scat}}^2, \qquad \sigma_{bc} = -\frac{0.21}{L} \cdot \sigma_{\text{scat}}^2$$

as above those variances can be propagated onto the angular and p_t resolution:

$$\frac{\sigma_{p_t}}{p_t} = 1.2 \cdot \frac{\sin\theta}{0.3\,B} \cdot \frac{14\,\text{MeV}/c_{light}}{L} \sqrt{\frac{L}{X_0}},$$

$$\sigma_\varphi = \sigma_{\text{scat}} \sqrt{(0.23 + 1.43\,\frac{x_{\text{vertex}}^2}{L^2} - 0.21\,\frac{x_{\text{vertex}}}{L})} \overset{\text{H1 vertex}}{\approx} 0.52 \cdot \frac{14\,\text{MeV}/c_{light}}{\beta \cdot p} \sqrt{\frac{L}{X_0}}$$

where θ is the angle of the particle with respect to the magnetic field or the polar angle. The last approximation is valid for a vertex position $x_{\text{vertex}} = -0.25L$.

The expressions shown above account for the multiple scattering happening inside the tracking detector. The track angle uncertainty is increased further when material in front of the tracker is leading to multiple scattering (scattering angle varaince given by σ_{scat}^2). The contributions from the finite space point resolution and from MS before and inside the tracker have to be added in quadrature.

A.3. Application

In figure A.2 the theoretical transverse momentum and angular resolution of the central and forward tracking system are shown. The plots are obtained using the number given in table A.1. The CJC-1 and 2 weighted mean curve is showing the obtainable resolution when measuring p_t in each chamber individually and calculating the weighted mean of both values (thus avoiding

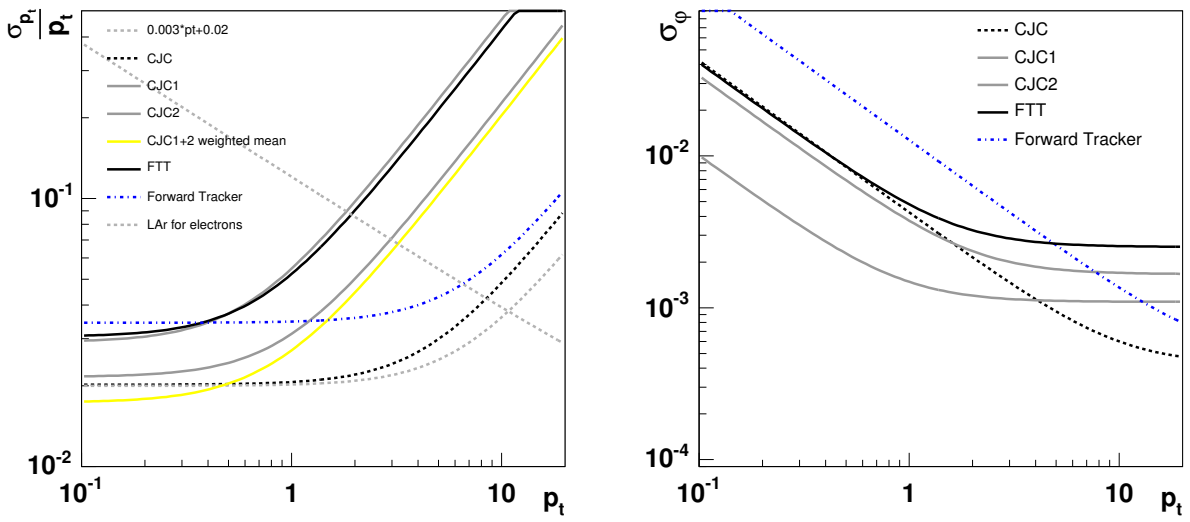

Figure A.2.: Theoretical Momentum (left) and angular(right) resolution of the H1 tracking system.

the loss of resolving power due to MS between the chambers) . The angle measurement cannot be improved this way, because direction variations in or before CJC-1 affect the outer chamber of course in a correlated way. The FTT hit resolution is taken from section 4.6. The expected p_t resolution obtained with these numbers is $\frac{\sigma_{p_t}}{p_t} \approx 0.03\text{GeV} + 0.04 \cdot p_t[\text{GeV}]$, which is in agreement with the results obtained in the FTT simulation [34].

Table A.1.: H1 Tracking: Parameters relevant for resolution calculation.

The amount of materials is estimated from the following numbers[X_0]: thickness of CST 1.5% [44], CIP 1% [45], angular resolution between CJC-1 and CJC-2 is compatible with 2% inside each CJC and 3% in between them (status 2000) [46], thickness of FTD planar chamber 1% new, and slightly more ($\sim$1.5%) for old ones [47], compare also dead material distribution in [25], figure 6.

	CJC-1	CJC-2	Forward Tracking Detector	FTT Readout
θ-acceptance:				
maximal	11° to 170°	26° to 154°	7° to 25°	30° to 150°
full B integral		40° to 140°	15° to 25°	
Resolution	150μm	150μm	200μm[48]	325μm
wire layers	24	32	5x6+9x4=66	12
$r\varphi$-track length	0.84m-0.53m	0.45m-0.22m	0.75m-0.15m	0.6m-0.22m
material [X_0]:				
before detector	3%	8%	50%[47]	4%
inside tracker	2%	2%	19%	6%

B. Data Processing

In the following subsections detailed information about the data handling on the front end module and merger is given. Emphasis is placed on the notion of the data that is read out for monitoring and debugging purposes. In particular the names of the BOS banks[1] written on raw data tapes are introduced.

B.1. Front End Modules

The analogue input from the buffer cards, that are attached to the standard CJC readout system, is digitized and fed to the F-FPGAs. The Qt algorithm running here identifies peaks in the wire current, determines their point in time and calculates the deposited charge for each wire end[2] as well as the corresponding z position. The result from the algorithm is stored in the TT0H Bank, which is read out by default. For further studies the raw data Banks TTRD or TTRH containing FADC output can be recorded in dedicated runs.

When a hit is found an entry is filled in the shift register associated with the corresponding wire, that has a depth of approximately 120 Bit (= 15 bunch crossings). With a frequency of 83.3 MHz all register entries are shifted by one bit, such that the drift time of the hit is encoded in the bit position. The z information is stored in parallel shift registers. All shift registers can be read out from the F-FPGA and are stored in the TT1R bank, in that case.

The identification of track segments can now be performed by comparing the registers holding the time information with precalculated patterns, so called *masks*. The masks are defined by the state of precalculated shift registers at a definite time after the passing through of a vertex fitted track. This point in time is given by the maximal drift time of all FTT wires ($\sim$ 9 BC compare subsection 2.2.3 on page 11) and is defined during the mask calculation. Thereby also the time-lag between the bunch crossing of origin a *measured* track and the time of validity of the mask is determined.

B.1.1. L1 Phase

At L1 the shift registers are only evaluated with an accuracy of 20.8 MHz (48 ns), which is achieved by combining four adjacent register entries with logical 'OR' before the mask comparison. Thereby the number of valid masks is reduced to a number which can be be handled by CAMs on the F-FPGA having a capacity of 3072 masks. The five shift registers of one trigger group are divided into subsets each comprising parts of three relevant shift registers, accounting for the fact that segments contain exactly one hit per wire layer. The register subsets are classified according to 'in-cell' and 'left-' or 'right-neighbouring' and compared to masks correspondingly. More details are described in [34].

The pattern identification is repeated every bunch crossing, leading to valid and in particular linkable track segments only in the case of a correct T_0 hypothesis [3].

[1] identifiable as capital 'four-letter' words.

[2] The unit of the charge calculated by the Qt algorithm is defined by the FADC and happens to fulfill $Q^{\mathrm{hit}}_{\mathrm{FTT}} \approx 1.3 Q^{\mathrm{hit}}_{\mathrm{CJC}}$.

[3] For the definition of the T_0 hypothesis compare section 2.3 on page 13.

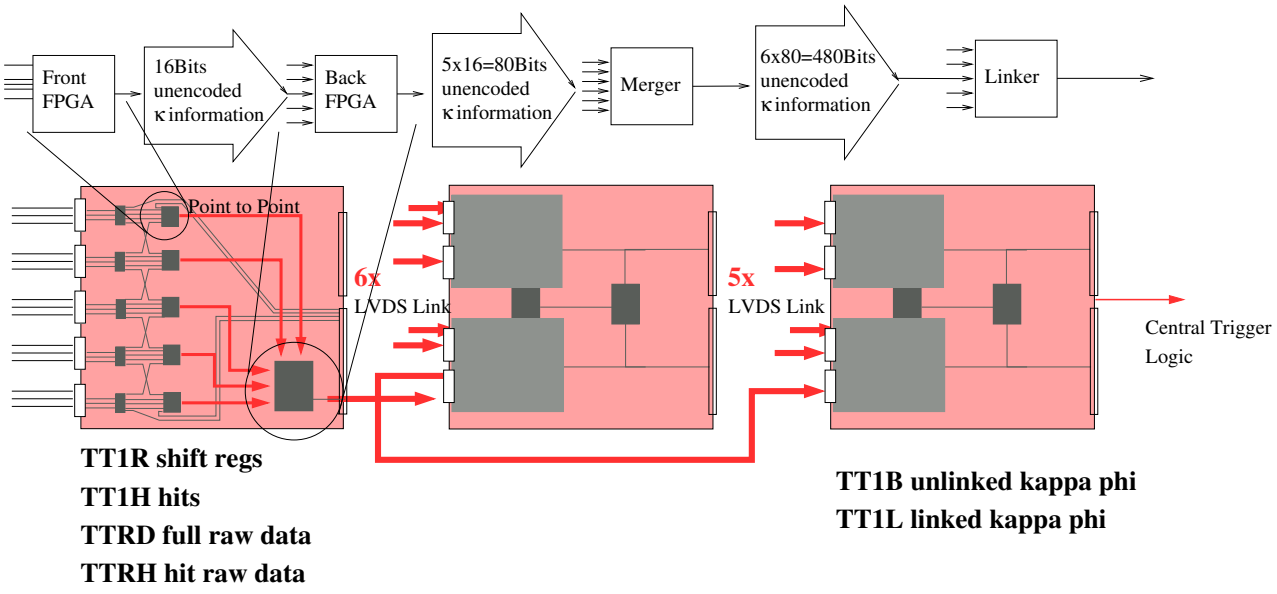

Figure B.1.: Overview over the L1 Data Path

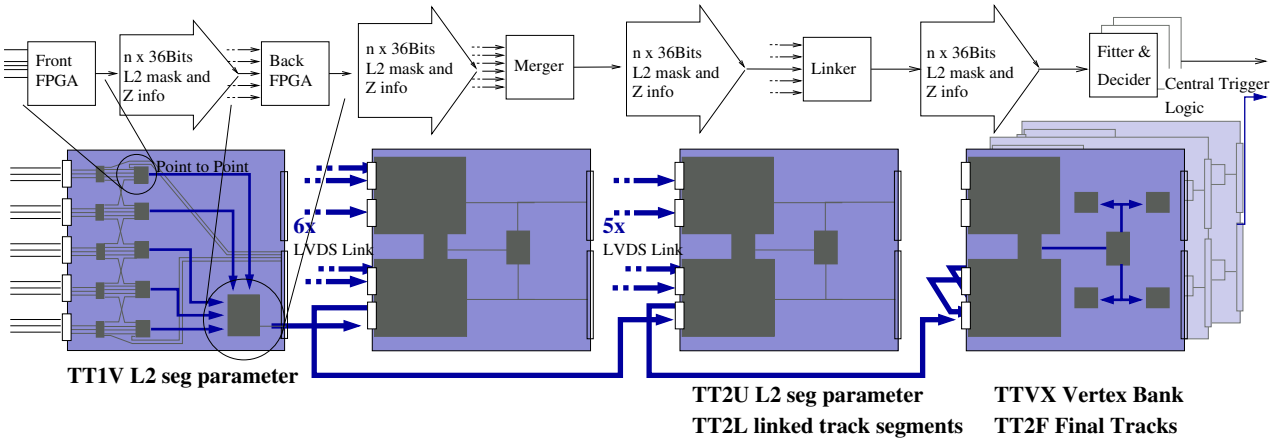

Figure B.2.: L2 Data Path

The κ values of all valid L1 Segment of a cell are calculated from the mask numbers and stored into an unencoded[4]16 bit word. This word representing a complete φ sector of the linker histogram is sent together with a validity bit to the L1-Merger and Linker chain via the B-FPGA. The φ value is regained later at the L1-Linker from the cell (and layer) number, that is encoded in the position of the *segment* in the data stream.

B.1.2. L2 Phase

For the L2 trigger decision the track segments are refined and validated. *Refinement* means adding the until then unused 83.3 MHz timing information. Only $\mathcal{O}(50\%)$ of the refined segments point to the interaction vertex to the increased precision, the rest is discarded in during the *validation* step.

[4]Unencoded meaning here that 16 bits represent 16 bins of a histogram each bin containing zero or greater equal than one entries.

After the L1Keep signal was received all shift registers are halted. The entries associated with the bunch crossing upon which the signal was issued have been shifted to a certain position defined by the L1 latency. This has to be accounted for by the L2 firmware.

In order to prepare the refinement the L1 mask number is translated into a 12bit number encoding the p_t of the segment. High p_t segments are refined and validated first, because only a fixed number of 128 segments per merger can be submitted to the linker. The 12 bit number is used to look up the shift register addresses (hit positions) needed for the actual access to the refinement information. The information from the shift registers is passed to the B-FPGA[5] and read out into the TT1U bank.

Here two look-ups are performed using the 83.3 MHz mask number consisting of the 12bit p_t or priority encoding number and of the 6bit timing refinement. The first look-up validates the vertex constraint while the second is used to gain the coordinates κ, φ and d_{ca} of verified masks. The coordinates are passed to the merger chain and are written out in the TT1V bank.

B.1.3. Z-Segments

The planned z-vertex trigger extension of the FTT uses available resources at the B-FPGA to perform a segment finding in the $r-z$ plane. During the pre-L1Keep time z information stored in shift registers on the F-FPGA is transmitted to the B-FPGA and a segment finding algorithm is started. Information from the $r-\varphi$ algorithm is used to implement a p_t cut, rejecting segments originating possibly from secondary vertices. The accepted z segments are sent via the merger cards to a dedicated z-linker MPB board.

B.2. The Merger

The Merger is implemented on a MPB using two Input/Input and two Input/Output piggy back cards. The merger is collecting information from six FEMs and passes it to the respective linkers (L1-, L2- and Z-Linker). The Merger is the second and only other stage in the FTT data path that is used commonly for L1 and L2 triggering and hence has to operation modes. Although the merger has a rather simple and well defined task the firmware is far from being trivial because of the very tedious timing requirements of especially the L1 part.

B.2.1. L1 Mode

In L1 Mode the six input streams are merged into two continuous output data streams. The six times 80 bits containing κ information from the L1 track segments are adding up to the number of 480 bits per bunch crossing. This corresponds to the maximal bandwidth, that can be transmitted over a LVDS channel link. This means a continuous bit stream of κ histogram rows is sent out to the linker, leading to special timing requirements for the whole system. In addition, the 720 bit unencoded z information has to be reduced for the transmission during one bunch crossing. This is done by combining the z histograms of certain adjacent cells with logical 'OR' , compare also figure B.3. Thereby the partition of the φ range in 30 cells is reduced to ten sectors for the z vertex trigger.

B.2.2. L2Mode

During the L2 Mode the 83.3MHz track segments have to be transmitted from the FEMs to the Fitter, where the full hit information is needed. Each L2 segments consist of one LVDS

[5] Comprising 18 bits z information, 12 bit priority encoding number and 6 bit timing refinement.

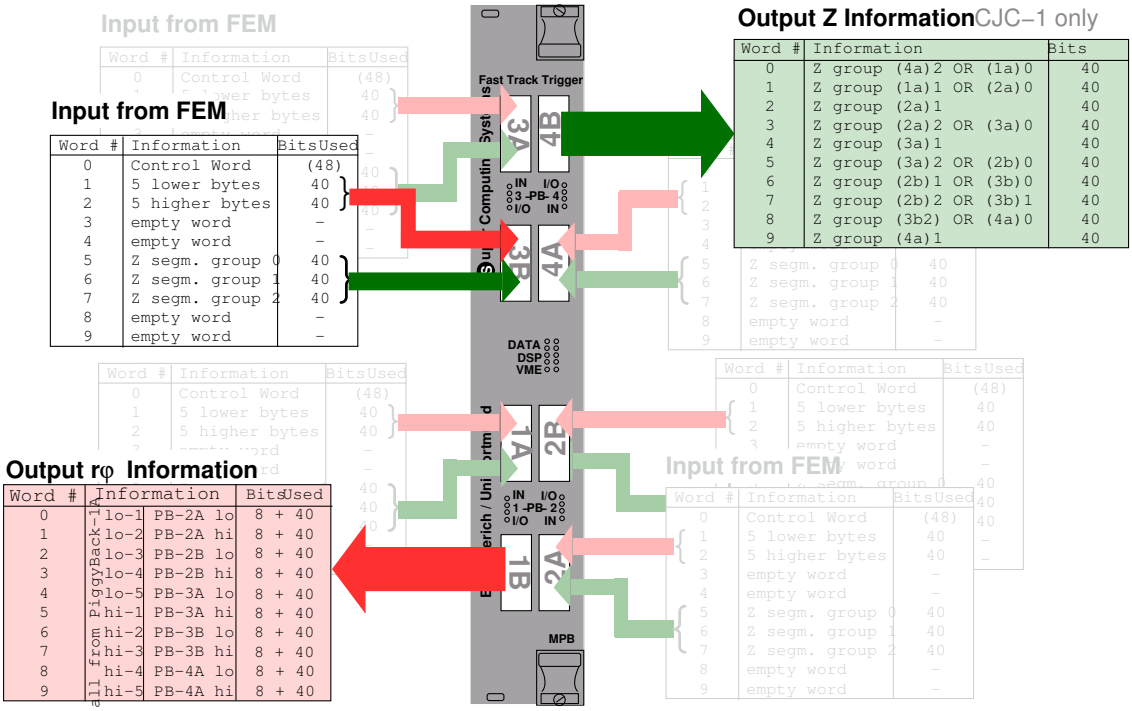

Figure B.3.: The L1 mode of the merger. The input streams of six FEMs are merged to one $r-\varphi$ segment stream and one stream being sent out to the z-Linker.

word of 48 bit depth, to be compared with the L1 segments represented by an entry in the transmittedκ histogram rows. Up to 128 L2 segment words per merger accompanied by a leading and terminating control word are sent to the L2-Linker.

B.3. Hardware

The Hardware of the FTT uses some special signal and data processing techniques briefly described here.

FPGA Field programmable gate arrays are high density electronic components that provide the possibility to apply a programmable logic to digital signal lines. Input or output connections and complex grids of logical gates are assigned to several hundreds of i/o pins. Implementations of standard components such as RAM-memories, adders, FIFOs, CAMs and so on can be found in libraries. FPGAs are operated at frequencies of typically 100 MHz or more and allow the parallel processing of big amounts of data.

CAMs content addressable memories are basically 'inverse memories'. Instead of feeding an address value and getting the content of the memory cell a content value is fed to the CAM and one or more addresses cells containing the content are read back. This technique is used in the L1 trigger for a fast look-up of the hit patterns. Compared to a standard look-up table CAMs are much more efficient since only valid entries have to be stored.

LVDS Bus The data transfer between the different electronic boards of the FTT is realized using the 'Channel Link' system from National Semiconductor [49]. Data Words with a depth of 48 bits are transmitted through nine multiplexed differential signal lines in point

to point connections. Each differential signal is transmitted over two lines by transmitting the inverse signal over the second line and measuring the difference of both lines at the receiver. The more stable and with precise timing receivable signal enables the Channel Link to be operated at 104 MHz and thus provide a bandwidth of $\sim$5 GBit/s.

FPDP Bus The Front Panel Data Port bus is used for the point to multipoint transfers needed in the L3 system. It is a platform-independent 32-bit synchronous data flow path that allows data to be transfered at high speeds (160 MBytes/sec.) [50]

VME_Bus The Versa Modul Eurocard bus is a widely used backplane bus for electronic crates (standardisation IEEE 1014-1987)

Bibliography

[1] D. H. Perkins, *Introduction to High Energy Physics.* Cambridge University Press, Cambridge, 2000. 4th edition.

[2] F. H. an Alan D. Martin, *Quarks and Leptons: an Introductory Course in Modern Particle Physics.* Wiley, 1984.

[3] R. W. Mcallister and R. Hofstadter, *Elastic scattering of 188-MeV electrons from the proton and the alpha particle* Phys. Rev. **102** (1956) 851–856.

[4] R. Hofstadter, F. Bumiller, and M. R. Yearian, *Electromagnetic Structure of the Proton and Neutron* Reviews of Modern Physics **30** (1958) 482–497.

[5] W. K. H. Panofsky, *Electromagnetic interactions: low q**2 electrodynamics: elastic and inelastic electron (and muon) scaterring.* Presented at 14th Int. Conf. on High Energy Physics, Vienna, Aug 1968.

[6] M. Breidenbach *et al.*, *Observed behavior of highly inelastic electron - proton scattering* Phys. Rev. Lett. **23** (1969) 935–939.

[7] J. D. Bjorken, *Theoretical ideas on high-energy inelastic electron proton scattering.* Invited paper at the Amer. Phys. Soc. New York Meeting, Feb 3, 1969.

[8] R. P. Feynman, *Very high-energy collisions of hadrons* Phys. Rev. Lett. **23** (1969) 1415–1417.

[9] J. D. Bjorken and E. A. Paschos, *Inelastic electron proton and gamma proton scattering, and the structure of the nucleon* Phys. Rev. **185** (1969) 1975–1982.

[10] D. H. Perkins, *Review of neutrino experiments.* In *Stanford 1975, Symposium On Lepton and Photon Interactions At High Energies*, Stanford 1975, 571-603.

[11] D. J. Fox *et al.*, *Test of scale invariance in high-energy muon scattering* Phys. Rev. Lett. **33** (1974) 1504.

[12] **H1** Collaboration, C. Adloff *et al.*, *Measurement and QCD analysis of neutral and charged current cross sections at HERA* Eur. Phys. J. **C30** (2003) 1–32, `hep-ex/0304003`.

[13] J. Callan, Curtis G. and D. J. Gross, *High-energy electroproduction and the constitution of the electric current* Phys. Rev. Lett. **22** (1969) 156–159.

[14] **H1** Collaboration, C. Adloff *et al.*, *Deep-inelastic inclusive e p scattering at low x and a determination of alpha(s)* Eur. Phys. J. **C21** (2001) 33–61, `hep-ex/0012053`.

[15] **H1** Collaboration, C. Adloff *et al.*, *Inclusive D0 and D*+- production in neutral current deep inelastic e p scattering at HERA* Z. Phys. **C72** (1996) 593–605, `hep-ex/9607012`.

[16] U. Schneekloth, *The HERA luminosity upgrade.* DESY-HERA-98-05.

[17] M. Seidel, *HERA luminosity upgrade.* Prepared for IEEE Particle Accelerator Conference (PAC 99), New York, NY, 29 Mar - 2 Apr 1999.

[18] E. Gianfelice-Wendt *et al.*, *Longitudinal Positron Polarisation in HERA-II* 2004. MOPLT044.

[19] **H1** Collaboration, I. Abt *et al.*, *The H1 detector at HERA* Nucl. Instrum. Meth. **A386** (1997) 310–347.

[20] **H1** Collaboration, I. Abt *et al.*, *The Tracking, calorimeter and muon detectors of the H1 experiment at HERA* Nucl. Instrum. Meth. **A386** (1997) 348–396.

[21] M. Fleischer, *The performance of the H1 liquid argon calorimeter.* One of three related talks included in DESY-98-005 and given at the 7th International Conference on Calorimetry in High-Energy Physics (ICCHEP 97), Tucson, AZ, 9-14 Nov 1997.

[22] H. Hutter, *Teststrahl-Untersuchungen an einem Spaghetti-Kalorimeter für den H1-Detektor* Master's thesis, Universität Dortmund, 1995.

[23] E. Tzamariudaki, *Performance of the H1 lead/scintillating-fibre calorimeter.* One of three related talks included in DESY-98-005 and given at the 7th International Conference on Calorimetry in High-Energy Physics (ICCHEP 97), Tucson, AZ, 9-14 Nov 1997.

[24] D. Reyna, *Modifications to SpaCal for H1 High Luminosity Operation and the Effect on Acceptance* H1 internal note H1-11/98-555, 1998.

[25] **H1 Calorimeter Group** Collaboration, B. Andrieu *et al.*, *The H1 liquid argon calorimeter system* Nucl. Instrum. Meth. **A336** (1993) 460–498.

[26] D. Pitzl, *some CJC studies* talk on H1 tracking group meeting 01-05-2005, 2005.

[27] C. Wissing, *Enwicklung und Test der dritten H1-Triggerstufe.* PhD thesis, Universität Dortmund, 2003.

[28] D. Wegener, *Skript zur Vorlesung Teilchendetektoren* 2001. Universität Dortmund.

[29] T. Nicholls *et al.*, *Concept, design and performance of the second level trigger of the H1 detector* IEEE Trans. Nucl. Sci. **45** (1998) 810–816.

[30] K. Urban, *Triggerstudien für eine Messung der Protonstrukturfunktion F_2 bei H1* Master's thesis, Universität Dortmund, 2005.

[31] J. Naumann, *Enwicklung eines Simulationsprogramms und Implementierung schneller Spurfitalgorithmen für den neuen H1-Driftkammertrigger.* PhD thesis, Universität Dortmund, 2003.

[32] T. Wolff *et al.*, *A Drift chamber track finder for the first level trigger of the H1 experiment* Nucl. Instrum. Meth. **A323** (1992) 537–541.

[33] S. Eichenberger *et al.*, *A fast pipelined trigger for the H1 experiment based on multiwire proportional chamber signals* Nucl. Instrum. Meth. **A323** (1992) 532–536.

[34] Y. H. Fleming, *The H1 First Level Fast Track Trigger.* PhD thesis, University of Birmingham, 2003.

[35] V. Karimaki, *Effective circle fitting for particle trajectories* Nucl. Instrum. Meth. **A305** (1991) 187–191.

[36] D. Meer, D. Muller, J. Muller, A. Schoning, and C. Wissing, *A multifunctional processing board for the fast track trigger of the H1 experiment* IEEE Trans. Nucl. Sci. **49** (2002) 357–361, `hep-ex/0107010`.

[37] A. Schoening, *Description of the FTT merging scheme* FTT Document, last updated 01-2005, 2005.

[38] N. B. Andre Schoening, *Description of the FTT L2 Decider* FTT Document, last updated 03-2005, 2005.

[39] A. Jung, *Inbetriebnahme der dritten Stufe des schnellen Spurtriggers für das H1-Experiment* Master's thesis, Universität Dortmund, 2004.

[40] V. Blobel and C. Kleinwort, *A new method for the high-precision alignment of track detectors* `hep-ex/0208021`.

[41] V. Blobel, *Millepede: Linear Least Squares Fits with a Large Number of Parameters* available at http://www.desy.de/ blobel/wwwmille.html.

[42] T. S. Corporation, *The Industry Leading VMEbus-to-PCI Bus Bridge* http://www.tundra.com/Products/Bridges/UniverseII/.

[43] R. L. Gluckstern, *Uncertainties in track momentum and direction, due to multiple scattering and measurement errors* Nucl. Instrum. Meth. **24** (1963) 381–389.

[44] B. List, *The H1 Silicon Tracker* tech. rep., Inistitute for Particle Physics ETH Zuerich, 2002. ETHZ-IPP PR-2002-02.

[45] D. Baumeister *et al.*, *Progress Report on CIP and Level 1 Vertex Trigger, Addendum* tech. rep., H1, 1998. related to DESY-PRC-02.

[46] D. Pitzl, *CJC Resolution 2000* talk on H1 tracking group meeting 01-26-2005, 2005.

[47] **H1** Collaboration, *Proposal for an Upgrade of the H1 Forward Track Detector for HERA 2000* tech. rep., H1, 1998. DESY-PRC-98-06.

[48] P. Laycock, *FTD Status Report* talk on H1 Technical Plenary meeting 06-16-2004, 2004.

[49] National Semiconductor Corporation, *48-Bit LVDS Channel Link SER/DES – 33 - 112 Mhz* Version 2002. DS90CR483/DS90CR484 http://www.national.com.

[50] I. Circuits and I. Systems Ltd., *The Front Panel Data Port Bus* http://www.fpdp.com.

Danke

Ich möchte hier allen danken, die mit ihrem Wohlwollen oder ihrer konkreten Hilfe zum Gelingen dieser Arbeit beigetragen haben. Allen voran meiner stets gut gelaunten Mutter, die seit ich denken kann darauf hingearbeitet hat, dass alle ihre drei Söhne studieren können und auch wollen. Auch meiner Tante Maria möchte ich für viele inspirierenden Gespräche beim Familienessen danken.

Herrn Prof. Dr. D. Wegener gilt mein besonderer Dank für die Gelegenheit am DESY Diplomarbeit schreiben zu dürfen und für seine immer aufmunternde Art, mit der er die zahllosen Diplomanden auch besonders kurz vor Schluss unterstützt hat. Ich möchte Ihnen auch danken für Ihre legendäre Fähigkeit, Gutachten zu schreiben, die mich vor zwei Jahren bis nach Genf gebracht hat.

Herrn Prof. Dr. Hans-Christian Schultz-Coulon danke ich für die Bereitschaft die Aufgabe des Zweitgutachters zu übernehmen und für die wunderbar rauschenden Grill- und sonstigen Feste auf denen man willkommen war.

Christoph, der immer ein Quell des iX Betriebsystem-Wissens war danke ich für die Betreuung meiner Arbeit und für die Bereitschaft, um zwei vor zwölf noch konzentriert eine Korrektur zu lesen. Klaus Kleinwort möchte ich für seine vielen Erklärungen zu den CJC Kalibrationsmethoden danken. Mein Dank gilt auch dem FTT Team für die nette Gesellschaft: Ronnie, Raphael, Katja, Guillaume, Wenbiao, Martin und insbesondere Nik und Andre, für die ein oder andere Erläuterung über die verwirrenden Verstrickungen in der Front End Datenverarbeitung. Marc Oliver danke ich für die Hartnäckigkeit, mit der er versucht hat, mir eine zu korrigierende Version irgendeines Kapitels abzuluchsen und für die kritische Begutachtung des einen, bei dem er es geschafft hat. Den Dortmundern im Ganzen möchte ich für die freundliche Aufnahme in den Club de la cuisine a la Hochpreisel danken, auch wenn man mich dort in letzter Zeit vermisst hat. Wann immer es eine Airbus Frage zu ergooglen gab, wir waren dabei. Erwähnt werden soll auch Disko Olafs Auftritt im Perlhuhnkeller, wo der Teppich gerockt wurde. Und wenn wir schon beim Abendleben sind: die nette erweiterte Dortmunder Vogelrunde Mitch, Christopher, Andrea, Olli, Martin, ... bei der man ab und zu mal Dienstags ins Wohnzimmer vorbeigekommen ist, oder die man beim berühmten Grillen an der Elbe treffen konnte.

Ein besonderen Platz bekommt natürlich das Kicker Team meines Vertrauens, das wie es sich begibt, ganz in meiner Nähe wohnt: Chief Rocker am Tisch Klaus, Jörg der Gartenporschefahrer, Jesko der beim reden Haken schlägt, Stevie der immer für eine Überraschung gut ist, Andy der mit dem Holz tanzt und last but not least Wiki Mo: "Ich bin eine...". Durch gemeinsame (mit irgendwem hatte man es immer gemeinsam) Hochs und Tiefs in Hamburg Vorstadt, da freue ich mich doch aufs Allerheiligen Segeln, Andy ich bin dabei! oder war es Pfingsten oder...? Und dann ist es ja auch Zeit unserer achten Mitbewohnerin zu danken, der Klingel-Nancy: Danke für den seelischen Beistand beim Schreiben und viel Glück bei den Prüfungen! Und was kommt nach acht? Ja die neunte Mitbewohnerin (meine persönliche Nummer eins) und Hauptkorrekturleserin, der ich mich gar nicht traue einen blöden Namen zu geben, weil ich sonst ganz großen Ärger kriege... Tausend Dank! Ich weiss, wenn du zusammenschreibst egal was kommt, ich habs verdient.

Diese Arbeit wurde mit Mitteln des Bundesministeriums für Bildung & Forschung unter der

Projektnummer 05H14BEA/6 gefördert.